

HIGH-TEMPERATURE CERAMIC SUPERCONDUCTORS

For Period  
July 1, 1989 - Sept. 30, 1989

October 10, 1989

Prepared for:

OFFICE OF NAVAL RESEARCH  
800 North Quincy Street  
Arlington, Virginia 22217-5000

DARPA/ONR Contract N00014-88-C-0714

GA Project 3850

Prepared by:

K. S. Mazdiyasni, Program Manager (619) 455-4587

K. C. Chen

W. J. DeHope

D. M. Duggan

Y. R. Lin-Lui

F. C. Montgomery

S. S. Pak

R. B. Stephens

M. B. Maple, UCSD

L. Paulius, UCSD

P. K. Tsai, UCSD

DISTRIBUTION STATEMENT A

Approved for public release

Approved by:

T. D. Gulden

Director, Defense Materials

The views and conclusions contained in this quarterly report are those of the authors and should not be interpreted as necessarily representing the official policies, either expressed or implied, of the Defense Advanced Research Projects Agency of the U. S. Government.



**GENERAL ATOMICS**

89 10 26 055

AD-A214 251

## CONTENTS

1. INTRODUCTION . . . . .	1-1
1.1. Project Outline . . . . .	1-1
2. PROGRESS . . . . .	2-1
2.1. Sol-Gel Processing . . . . .	2-1
2.1.1. Materials Process Refinement . . . . .	2-1
2.2. Materials Synthesis and Characterization . . . . .	2-3
2.2.1. Yttrium and Rare Earth 123 Powders . . . . .	2-3
2.2.2. Morphology of $\text{YBa}_2\text{Cu}_3\text{O}_{7-x}$ Powders . . . . .	2-3
2.2.3. Effect of Refluxing . . . . .	2-9
2.2.4. Carbon Content . . . . .	2-9
2.2.5. Electrical Resistivity Measurements . . . . .	2-9
3. THIN FILMS COATING METHODS . . . . .	3-1
Method A . . . . .	3-1
3.1. Effect of Atmosphere . . . . .	3-1
3.2. Effect of Number of Coating Cycles . . . . .	3-1
3.3. Effect of Water/Solvent . . . . .	3-1
3.4. Superconducting Properties . . . . .	3-6
3.5. Thin Film Coating Method . . . . .	3-6
Method B . . . . .	3-6
4. FORMATION OF MICRO-INHOMOGENEITY FOR FLUX PINNING CENTERS . .	4-1
5. FIBER PREFERRED CRYSTALLOGRAPHIC-ORIENTATION (TEXTURING) . .	5-1
6. CAVITY Q FACTOR MEASUREMENTS . . . . .	6-1
7. REFERENCE . . . . .	7-1
APPENDIX: FLUX BUNDLE INTERACTIONS . . . . .	A-1

## FIGURES

1. Variation in sol rheology concentration as functions of water and solvent . . . . .	2-2
2. Typical morphology of a $\text{YBa}_2\text{Cu}_3\text{O}_{7-x}$ powder heat treated to 800°C in argon . . . . .	2-4

# FIGURES (Continued)

3. Morphology of a $\text{YBa}_2\text{Cu}_3\text{O}_{7-x}$ crystallite and its [001] diffraction pattern showing that it is tetragonal . . . . .	2-5
4. Transmission electron microscopy (TEM) photograph of a $\text{YBa}_2\text{Cu}_3\text{O}_{7-x}$ powder heat treated to $900^\circ\text{C}$ in flowing $\text{O}_2$ . . . .	2-6
5. XRD pattern and DTA thermogram of a $\text{YBa}_2\text{Cu}_3\text{O}_{7-x}$ powder heat treated to $900^\circ\text{C}$ in flowing $\text{O}_2$ . . . . .	2-7
6. Resistivity curve of a $\text{YBa}_2\text{Cu}_3\text{O}_{7-x}$ powder . . . . .	2-8
7. TEM image of a suspension obtained by refluxing . . . . .	2-10
8. SEM images of films obtained by coating in $\text{N}_2$ (top) and in air (bottom) . . . . .	3-2
9. SEM photographs of films coated once (top) and three times (bottom) in air . . . . .	3-3
10. SEM images of films obtained by coating once in air with sols whose $\text{H}_2\text{O}/\text{solvent}$ ratios are 0.0082 (top) and 0.0165 (bottom) . . . . .	3-4
11. SEM images of films obtained by coating once in air with sols whose $\text{H}_2\text{O}/\text{solvent}$ ratios are 0.0499 (top) and 0.0999 (bottom) . . . . .	3-5
12. Morphology of a film prepared from a sol which has been aged for 7 days . . . . .	3-7
13. $\text{Dy123}$ film on YSZ by single dipping . . . . .	3-9
14. Surface morphology of $\text{Dy123}$ film on YSZ . . . . .	3-10
15. $\text{Y123}$ film on YSZ with dive dippings . . . . .	3-11
16. The dc magnetic susceptibility of $\text{Y123}$ film on YSZ . . . . .	3-12
17. Critical current densities of $\text{Y123}$ film on YSZ at 5 and 50 K using Bean's model analysis . . . . .	3-13
18. Resistivity versus temperature plot of $\text{Y123}$ film on YSZ . . . .	3-14
19. X-ray diffractions of $\text{Y123}$ fibers with different amount of $\text{BaZrCuO}_5$ addition . . . . .	4-2
20. SEM micrographs of seeded $\text{Y123}$ fibers . . . . .	5-2

## TABLE

1. Resistive transitions of $\text{RBA}_2\text{Cu}_3\text{O}_{7-\delta}$ . . . . .	2-12
--	------

STATEMENT "A" per Dr. Wallace Smith ONR  
1 Nov 89 TELEOCN CG

Distribution	
Availability Codes	
Dist	Special
A-1	

## 1. INTRODUCTION

This is the fourth quarterly progress report on the work performed in the period from July 1, 1989 through September 30, 1989 on Office of Naval Research (ONR) Contract N00014-88-C-0714, entitled "High-Temperature Ceramic Superconductors." The principal objectives of this program are (1) to demonstrate fabrication of high-temperature ceramic superconductors that can operate at or above 90 K with appropriate current density,  $J_c$ , in forms useful for application in resonant cavities, magnets, motors, sensors, computers, and other devices; and (2) to fabricate and demonstrate selected components made of these materials, including microwave cavities and magnetic shields. JPS

### 1.1. PROJECT OUTLINE

This program has been divided into six tasks: (1) metal alkoxide synthesis and processing, (2) microstructural evaluation and property measurement, (3) electrical and magnetic property measurement, (4) superconductor ceramic processing, (5) component fabrication and demonstration, and (6) reporting.

Task 1 is to synthesize a homogeneous alkoxide solution that contains all the constituent elements which can be easily made to powders, thin film, or drawn into fiber form. Ideally, this solution should possess precise stoichiometry, adequate stability, polymerizability, adherence, and spinnability. Also, the polymeric materials formed from this solution should be thermosetting, be able to be dissolved in organic solvents and contain as little as possible low-temperature pyrolyzable organics with high char yield.

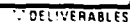
Task 2 is to study the microstructure as a function of processing parameters. The study includes: density, pore size and pore size distribution, phase identification, chemical composition and purity, environmental stability, effects of heat treatment, residual strain, seeding, annealing in magnetic fields, and epitaxy on grain growth and orientation.

Task 3 is to study the electrical and magnetic properties of the  $\text{YBa}_2\text{Cu}_3\text{O}_7$  (123) high  $T_c$  ceramic superconductors. It will include both the ac electrical resistance ( $R_{ax}$ ) and the ac magnetic susceptibility ( $\chi_{ac}$ ).

Task 4 is an investigation of superconductor ceramic processing. Most of the important applications of superconductors require material in the form of fiber or films. Magnets, conductors, motors, and generators are examples of applications employing fiber; while detectors, microwave cavities, and microcircuitry require superconducting material in the form of films. The sol-gel process is ideally suited to producing materials in these forms; in fact, it is used commercially to produce antireflection and mirror coatings, and to produce continuous ceramic fibers, for structural reinforcement in composite materials, and for thermal insulation.

Task 5 is to demonstrate component fabrication. General Atomics (GA) will design and build a high  $Q$ , high  $T_c$  superconducting cavity using its unique sol-gel coating process capabilities. This task would proceed after some initial coating tests verified dc superconductivity and questions of adhesiveness, surface preparation, and processing procedures are answered. As the fabrication process and the materials quality are improved throughout the three-year program, two additional cavities will be constructed and tested. Coupling would be through a waveguide inductive iris into an end wall with a logarithmic decrement technique of  $Q$  measurement being considered most appropriate for the

This report will focus mostly on Tasks 2, 3, 4, and 5.



## 2. PROGRESS

### 2.1. SOL-GEL PROCESSING

The type of sol required for fiber and/or thin film applications are different than that desired for powder synthesis. For powder synthesis, a suspension containing uniform submicron size precipitates with all three metals (Y, Ba, and Cu) distributed homogeneously would be ideal. This requires that all three metals precursor compounds hydrolyze simultaneously and rapidly. Thin films, on the other hand, require a homogeneous and stable sol. This requires a rather slow rate of hydrolysis. For these reasons, a major effort was concentrated during this reporting period in identifying critical experimental parameters that determine the rate of hydrolysis and the type of sol (or suspension) that results.

#### 2.1.1. Materials Process Refinement

A series of solutions were prepared by adding yttrium tris isopropoxide,  $Y(i-OPr)_3$ , and barium bis isopropoxide,  $Ba(i-OPr)_2$ , to a MeOH solution containing ammoniated copper bis methoxide,  $Cu(MeO)_2$ . Into the homogeneous solution, a predetermined amount of water and MeOH were added and the state of the resulting sol (or suspension) was observed.

From these experiments it was determined that the concentrations of the solvent and water are two of the most important processing parameters that must be carefully controlled and are the determining factor for the type of sol that results. A summary of the experiment is presented in Fig. 1. It can clearly be seen from this diagram that both a suspension meeting the proper requirements for powder synthesis and a sol needed for thin film formation could readily be prepared from the

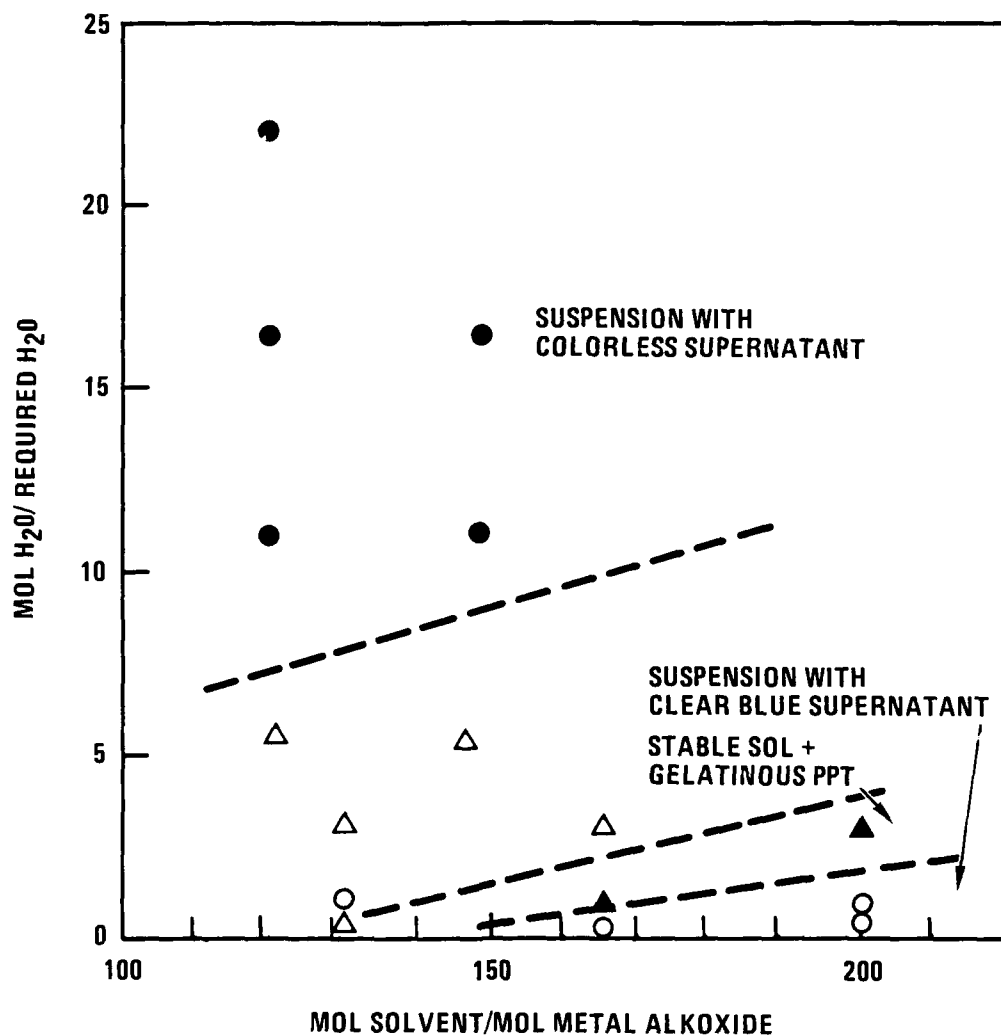


Fig. 1. Variation in sol rheology concentration as functions of water and solvent



same solution simply by controlling the amounts of water and the solvent.

## 2.2. MATERIALS SYNTHESIS AND CHARACTERIZATION

### 2.2.1. Yttrium and Rare Earth 123 Powders

The results obtained from Fig. 1 was used to prepare a suspension suitable for powder preparation in collaboration with UCSD. A typical procedure consist of hydrolyzing an ammoniated  $\text{Y}(\text{i-OPr})_3$  and/or  $\text{Ln}(\text{i-OPr})_3/\text{Ba}(\text{i-OPr})_2/\text{Cu}(\text{MeO})_2$  solution with at least 20 times the water required to fully hydrolyze all the metal constituents. The suspension was dried by rotary evaporation and calcined in flowing oxygen at  $900^\circ\text{C}$  (200 cc/min).

### 2.2.2. Morphology of $\text{YBa}_2\text{Cu}_3\text{O}_{7-x}$ Powders

Reference the work that was reported in the last progress report, the morphology of the  $\text{YBa}_2\text{Cu}_3\text{O}_{7-x}$  powders were monitored as a function of calcination temperature. Figure 2 shows a typical agglomerate that resulted when a powder sample was heat treated to  $800^\circ\text{C}$  in argon. It consists of fine particles that are approximately 100 to 200 nm in diameter. A diffraction analysis performed on an isolated 123 crystallite revealed that it is tetragonal and in [001] orientation (Fig. 3).

Similar powder morphology was observed (Fig. 4) when the powder was heated in oxygen. Agglomerate size and the individual crystallite size that make up the agglomerates were similar to the one given in Fig. 3.

Even though the powders are fairly pure (Fig. 5) and exhibit good superconducting properties (Fig. 6), their morphology is far from ideal for sintering and thus much work is needed to improve their quality.



0.5  $\mu\text{m}$

Fig. 2. Typical morphology of a  $\text{YBa}_2\text{Cu}_3\text{O}_{7-x}$  powder heat treated to  $800^\circ\text{C}$  in argon

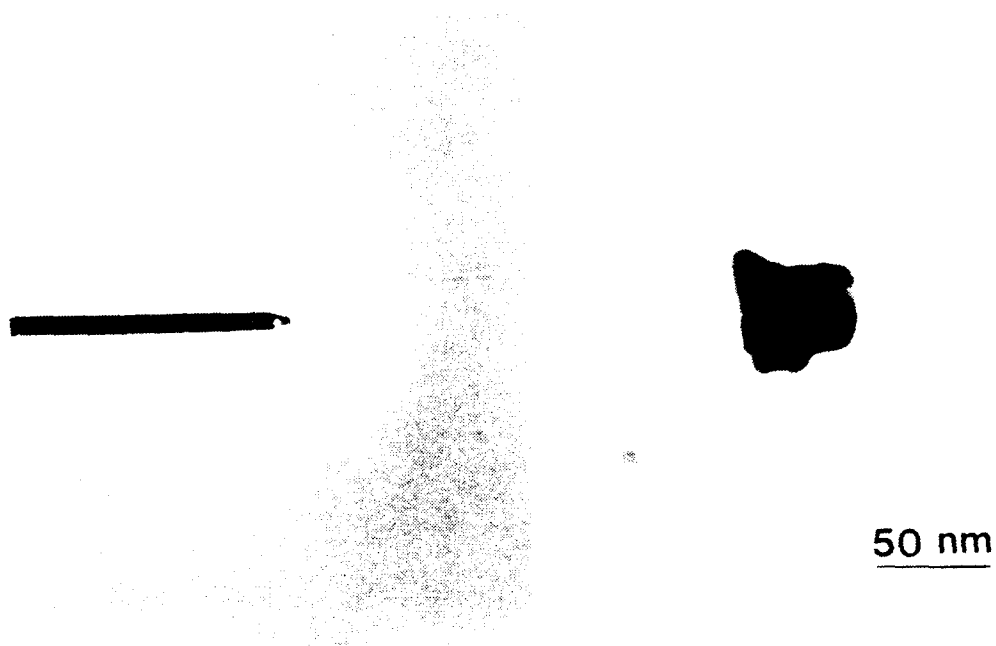


Fig. 3. Morphology of a YBa<sub>2</sub>Cu<sub>3</sub>O<sub>7-x</sub> crystallite and its [001] diffraction pattern showing that it is tetragonal



0.5  $\mu\text{m}$

Fig. 4. Transmission electron microscopy (TEM) photograph of a  $\text{YBa}_2\text{Cu}_3\text{O}_{7-x}$  powder heat treated to  $900^\circ\text{C}$  in flowing  $\text{O}_2$

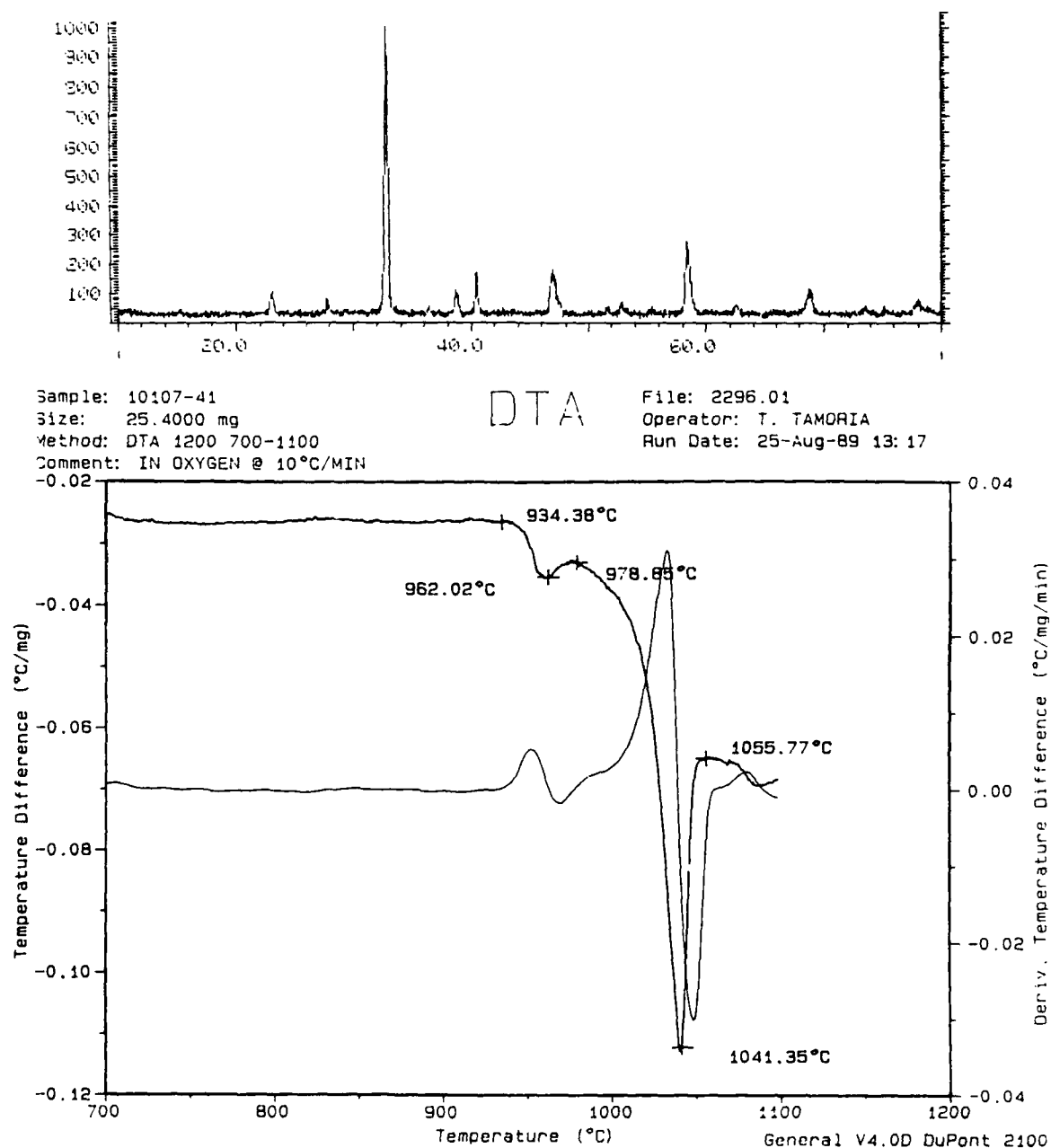


Fig. 5. XRD pattern and DTA thermogram of a  $\text{YBa}_2\text{Cu}_3\text{O}_{7-x}$  powder heat treated to 900°C in flowing  $\text{O}_2$

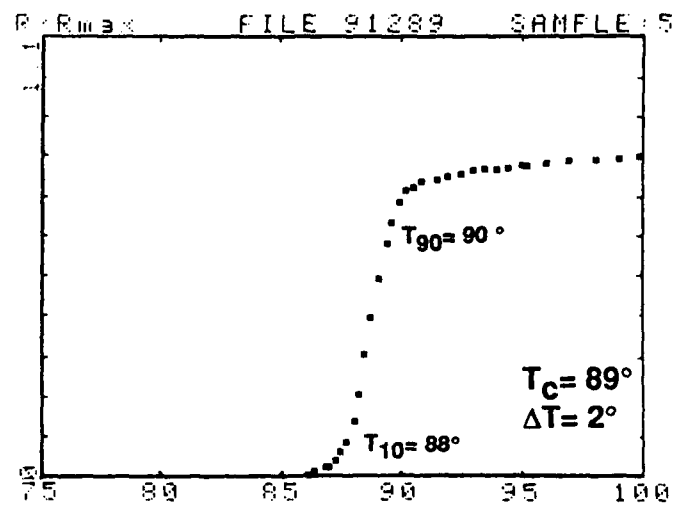


Fig. 6. Resistivity curve of a  $\text{YBa}_2\text{Cu}_3\text{O}_{7-x}$  powder

### 2.2.3. Effect of Refluxing

In the last report, it was mentioned that the size of as prepared particles are approximately 20 to 30 nm in diameter. It was thought that particles in this size regime are too active to prevent agglomeration during calcination. In an effort to reduce the severity of agglomeration, the as-prepared sol was refluxed for 72 h at the boiling temperature of MeOH. As shown in Fig. 7, the particles increased in size to approximately 500 nm in diameter by Ostwald ripening. The effect of their initial size difference on the morphology of the calcined powders are currently being investigated.

### 2.2.4. Carbon Content

Since residual carbon is known to be deleterious to superconductivity, an assessment of the concentration of carbon in the powder will serve as an indicator of the quality of the powder. A powder which has been calcined at 900°C for 1 h has been subjected to a combustion analysis. The results indicate that the carbon concentration is less than 0.031% by weight which is an order of magnitude greater than it is desired. Attempt is being made to reduce the concentration to a more acceptable level. For e.g., oxidative washing, using H<sub>2</sub>O<sub>2</sub>, is currently under investigation to further reduce the carbon concentration.

### 2.2.5. Electrical Resistivity Measurements

The rare earth powders RBa<sub>2</sub>Cu<sub>3</sub>O<sub>7-δ</sub>, where R = Er, Eu, Dy, Gd, Ho, Lu, Nd, and Sm were prepared in accordance with the procedures described in Section 2.2. The powders were pressed into pellets with a thickness of ~1 mm and annealed in flowing O<sub>2</sub>. Various annealing procedures were employed in an attempt to optimize the superconducting properties. After the pellets were cut into bars with cross sections of ~1 x 1 mm and lengths of ~8 mm, the electrical resistivity was measured as a function of decreasing temperature. The results for R = Er, Eu, Dy,

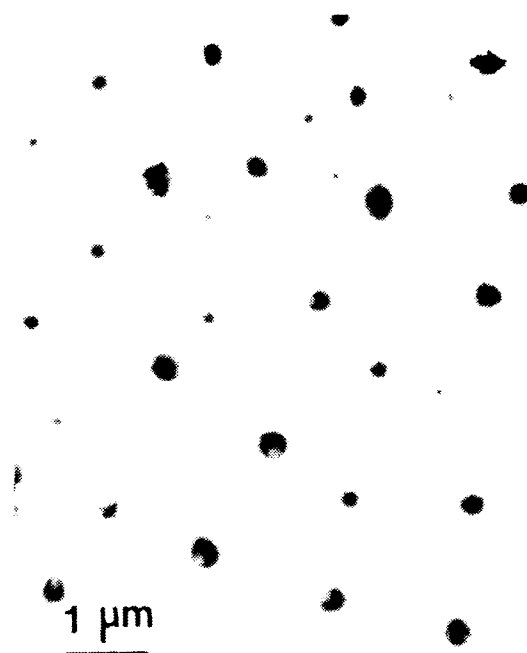


Fig. 7. TEM image of a suspension obtained by refluxing



Ho, and Nd are listed in Table 1. These samples had critical temperatures, defined as the resistive midpoint, from  $T_c = T_{0.5} = 84$  to 89 K, and transition widths, defined as the 10% to 90% resistive transitions, from  $\Delta T = T_{0.9} - T_{0.1} = 4$  to 7 K. Work is continuing on samples of  $\text{GdBa}_2\text{Cu}_3\text{O}_{7-\delta}$ ,  $\text{LuBa}_2\text{Cu}_3\text{O}_{7-\delta}$ , and  $\text{SmBa}_2\text{Cu}_3\text{O}_{7-\delta}$ .

Although comparison between samples is difficult because different rare earth compounds were measured, the highest and sharpest superconducting transitions appear to occur with the longest  $\text{O}_2$  anneals at 925° to 985°C.

TABLE 1  
RESISTIVE TRANSITIONS OF  $\text{R}\text{Ba}_2\text{Cu}_3\text{O}_{7-\delta}$

R	Annealing Procedure		$T_c$ (K)	$\Delta T$ (K)
	High Temperature	Low Temperature		
Er	46 h at 925°C	15 h at 425°C	89	5
Eu	48 h at 950°C	30 h at 430°C	85	5
Dy	46 h at 925°C	15 h at 425°C	87	5
Ho	24 h at 950°C	34 h at 430°C	84	7
Nd	60 h at 895°C	65 h at 430°C	88	4

### 3. THIN FILMS COATING METHODS

#### METHOD A

Two different chemical pathways deposition procedures are used and results are reported herein. Initial dip coating experiments prove that the viscosity of the homogeneous sols was too low for thick and smooth coatings. As an alternative, drops of the sols were placed on BaZrO<sub>3</sub> coated yttria stabilized zirconia (YSZ) substrates and let the wetting behavior of the sol to form a thick and smooth coating.

#### 3.1. EFFECT OF ATMOSPHERE

Two films were prepared from a sol (aged for seven days), whose molar solvent to metal ratio was 130:2 and contained one-half the water required to fully hydrolyze all the metals. One substrate was coated in dry N<sub>2</sub> while the other in air. Figure 8 shows clearly that the film obtained by coating in air is much superior to the one dried in N<sub>2</sub>.

#### 3.2. EFFECT OF NUMBER OF COATING CYCLES

In order to determine how many coating cycles are required to form a smooth film, YSZ substrates were coated once and three times with the same sol as the one used in Section 3.1 and fired to 900°C in flowing oxygen. The scanning electron microscopy (SEM) images in Fig. 9 show that one application gave a much smoother coating. A similar result was obtained in dry N<sub>2</sub> as well.

#### 3.3. EFFECT OF WATER/SOLVENT

Figures 10 and 11 show that there exists an optimum water to solvent ratio which yields a smooth and crack free films. In the

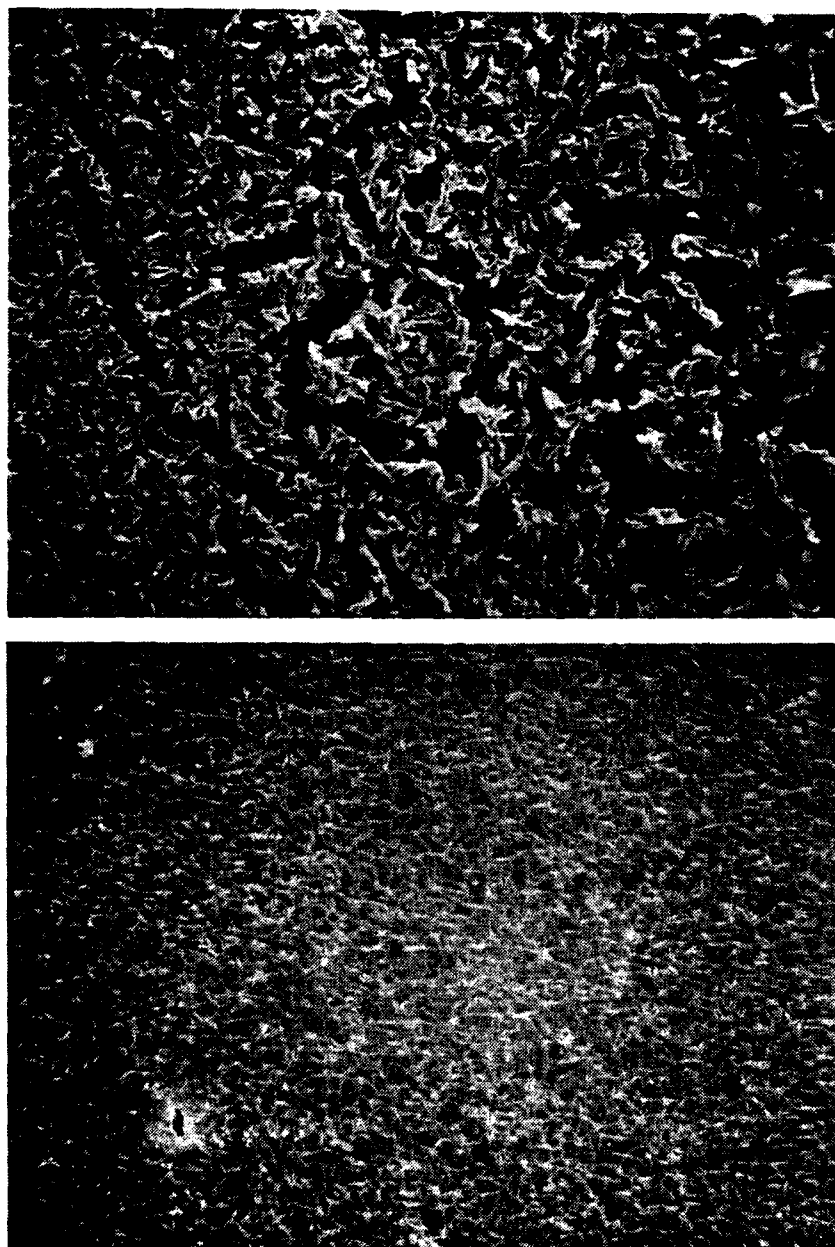


Fig. 8. SEM images of films obtained by coating in  $N_2$  (top) and in air (bottom)

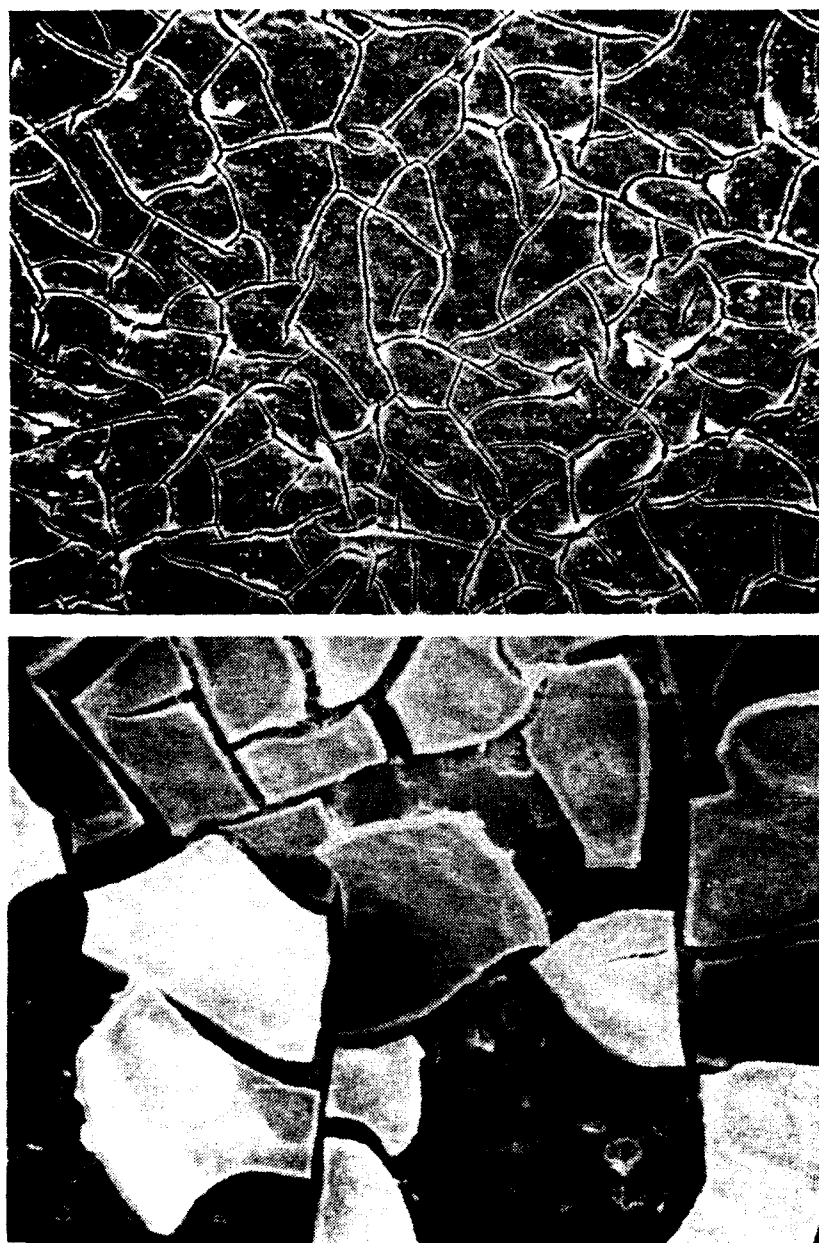


Fig. 9. SEM photographs of films coated once (top) and three times (bottom) in air

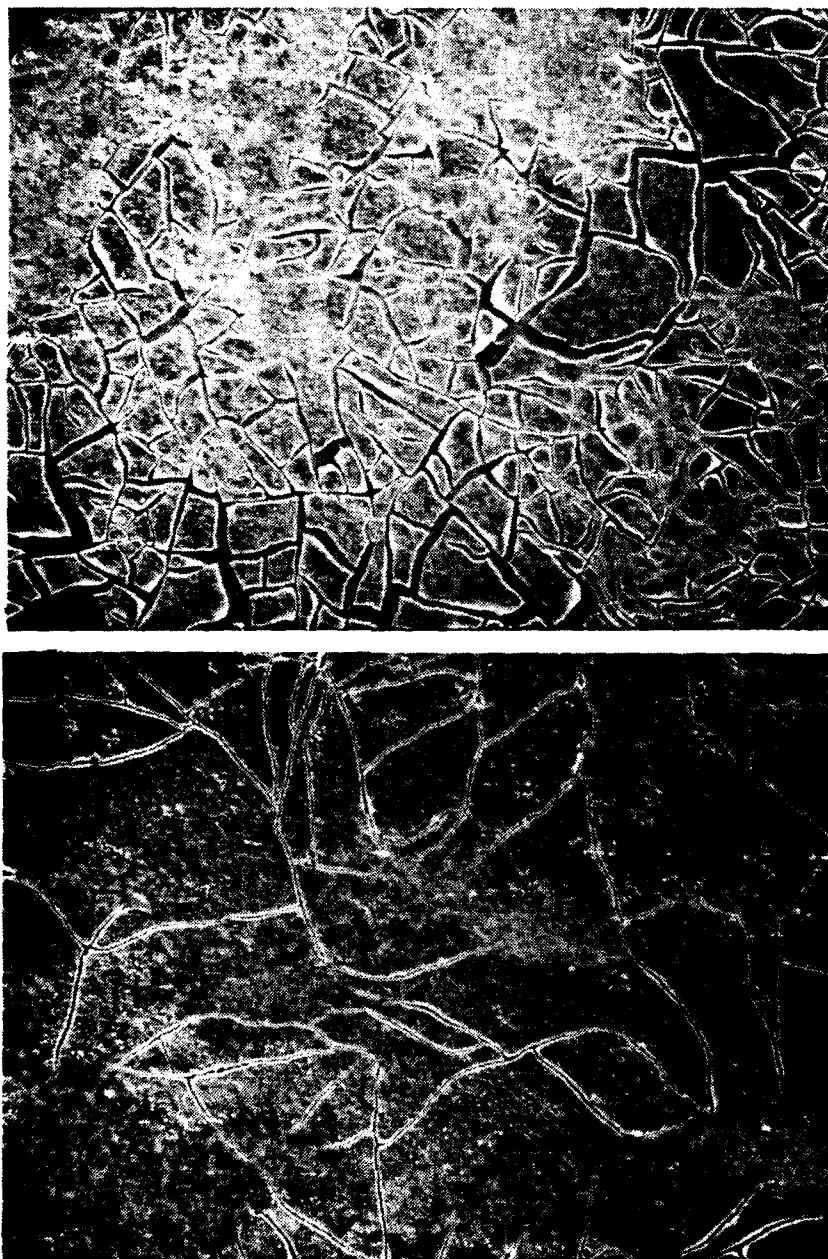


Fig. 10. SEM images of films obtained by coating once in air with sols whose  $H_2O$ /solvent ratios are 0.0082 (top) and 0.0165 (bottom)

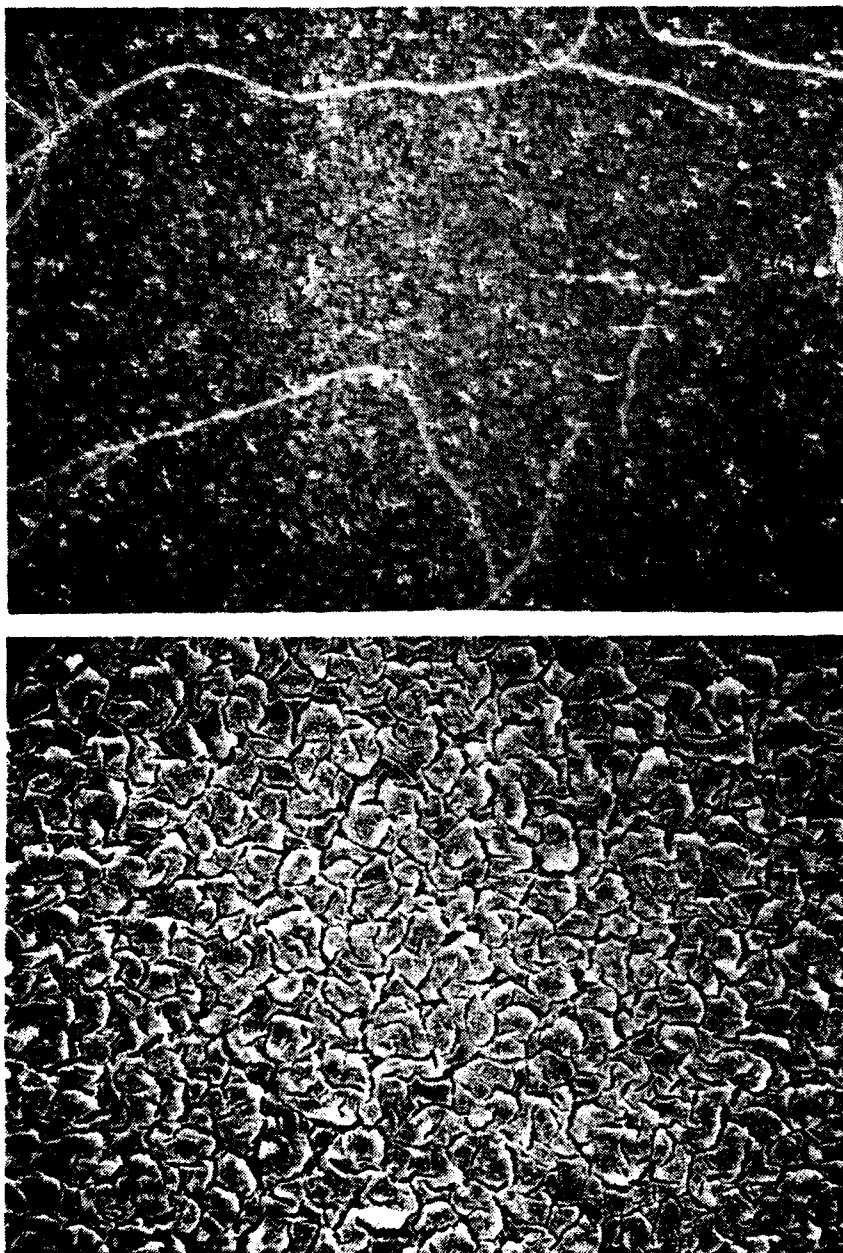


Fig. 11. SEM images of films obtained by coating once in air with sols whose  $H_2O$ /solvent ratios are 0.0499 (top) and 0.0999 (bottom)

compositions tested, the sol with water/solvent ratio equal to 0.05 gave the best result. However, additional work is needed to determine the significant of aging effect. Figure 12 shows a film that was obtained by aging the sol for seven days. A fairly smooth coating was obtained. However, when this sol is aged for more than 14 days, severe cracking can occur.

#### 3.4. SUPERCONDUCTING PROPERTIES

Up until now, the superconducting properties of the thin films by the above technique have not been satisfactory. A partial explanation could come from the following: a microprobe analysis of the film revealed that the ratio of Y:Ba:Cu is approximately 1:1.2:1.1. Invariably it appears that Ba and Cu react with the substrate and this behavior is consistent with the reactive nature of the film with YSZ substrates reported in the literature. A lower processing temperature for a shorter period of time might improve the results obtained at present.

#### 3.5. THIN FILM COATING METHOD

##### METHOD B

Thin films of 123 have been also prepared by dipping thin strips of YSZ in the dilute  $\text{YBa}_2\text{Cu}_3\text{O}_{7-x}$  and  $\text{DyBa}_2\text{Cu}_3\text{O}_{7-x}$  precursor solutions used for making 123 fibers. Thin barrier layer of  $\text{BaZrO}_3$  was applied to YSZ substrate prior to applying Y123 coating in order to prevent interaction between Y123 film with YSZ substrates during the crystallization and densification process. The  $\text{BaZrO}_3$  barrier coating solution was prepared by sol-gel method. Barium bis isopropoxide, zirconium n-propoxide and 2-ethylhexanoic acid in 1:1:3 molar ratio were mixed and used to make the  $\text{BaZrO}_3$  barrier layer. The X-ray diffraction of the powder made from this solution indicating pure  $\text{BaZrO}_3$ . The  $\text{BaZrO}_3$  films on YSZ was sintered at  $900^\circ\text{C}$  for 1 h to adherent crack free coating.



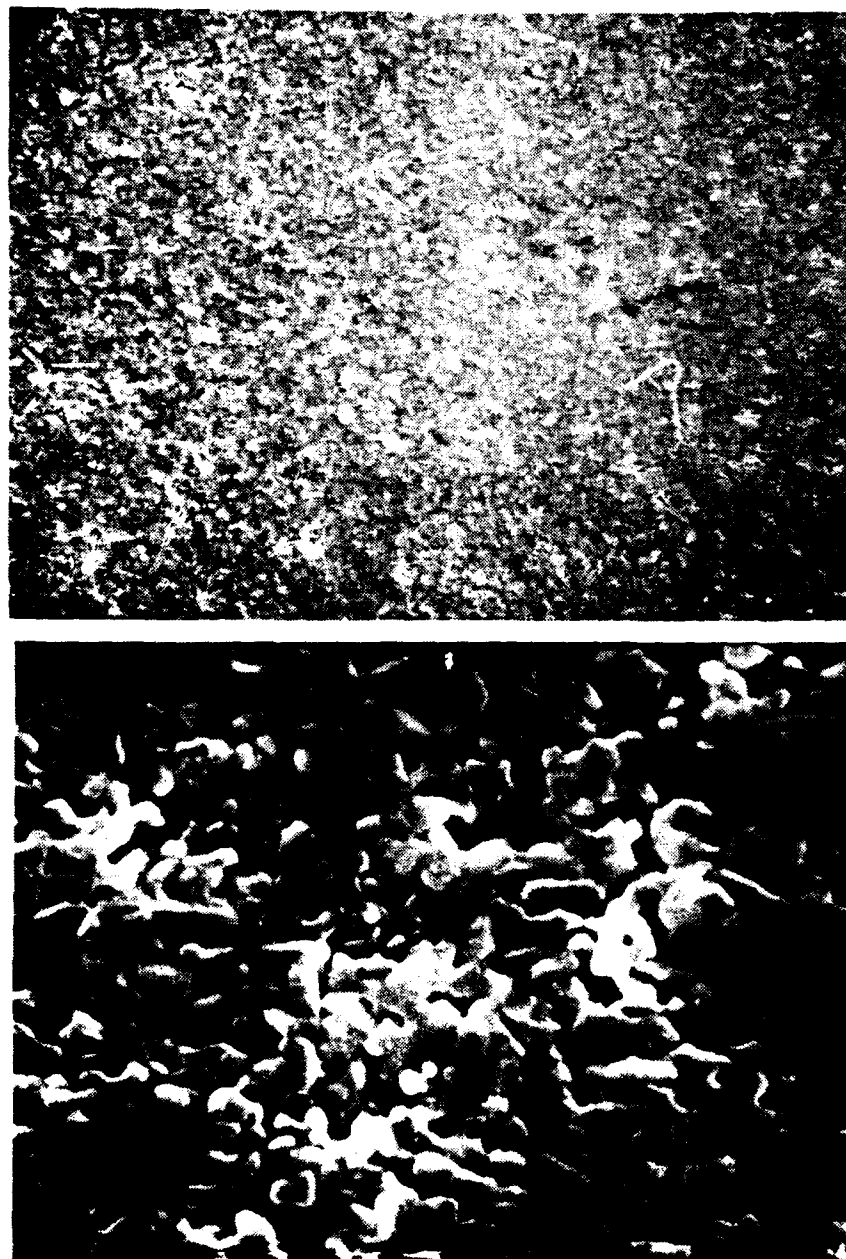


Fig. 12. Morphology of a film prepared from a sol which has been aged for 7 days

$\text{YBa}_2\text{Cu}_3\text{O}_{7-x}$  and  $\text{DyBa}_2\text{Cu}_3\text{O}_{7-x}$  films were then applied to  $\text{BaZrO}_3$ -coated YSZ substrates by dip coating process. Thickness of 0.8 micron was achieved by single dipping after firing at  $900^\circ\text{C}$  for 10 min (Fig. 13). At this thickness, no cracking was observed in the films (Fig. 14). The film thickness was increased by multiple dippings. Films were subjected to  $875^\circ\text{C}$  for 1 h after each dipping and when the desired thickness was achieved it was sintered at a final temperature of  $900^\circ$  to  $915^\circ\text{C}$ , for 10 to 30 min. Films of approximately 2 microns thick were obtained with five dipping cycles (Fig. 15). The thickness of the films does not linearly increase with the number of dipping cycles indicating refilling of the pores in the films by the subsequent dippings. At 2 micron thickness, the film exhibit cracks due to the large shrinkage during sintering. In order to optimize the coating thickness without cracking, the heat treatment schedule is being studied to prevent cracking, and enhance densification. The grain size of the coating obtained is approximately 0.4 to 1 micron with the mean average thickness being  $\approx 0.7$  microns.

Due to the low mass of the single dipped 123 film on YSIP substrate, the results of dc magnetic susceptibility measurement was not clear. However, the dc magnetic susceptibility measurement on the five-times-dipped films on the same substrate indicates the existence of superconducting onset transition temperature at approximately 85 K. The susceptibility versus temperature plot after correction for the London Penetration Depth is shown in Fig. 16. The critical current density calculation according to Bean's model at 5 and 50 K is given in Fig. 17. Due to micro-cracks in the film, the resistivity of the sample tested did not reach zero (Fig. 18).

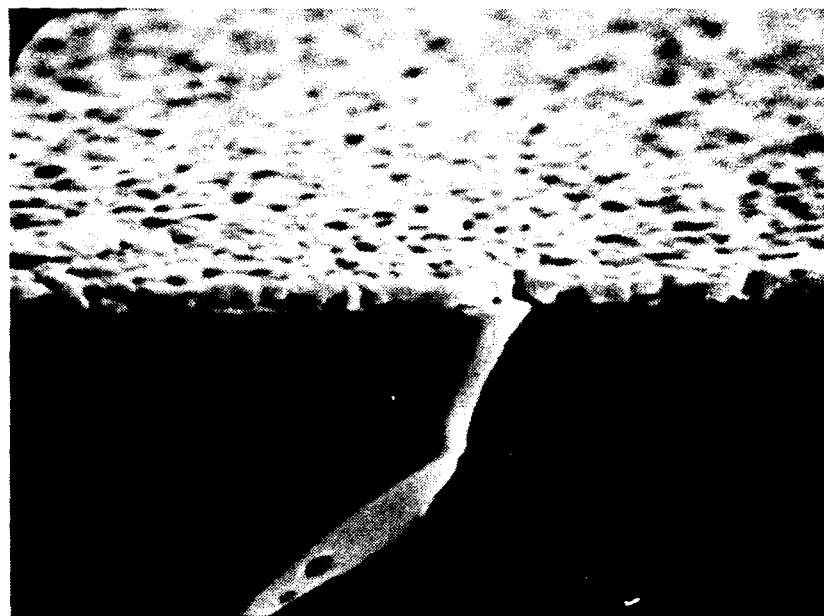


Fig. 13. Dyl23 film on YSZ by single dipping (900°C, 10 min)

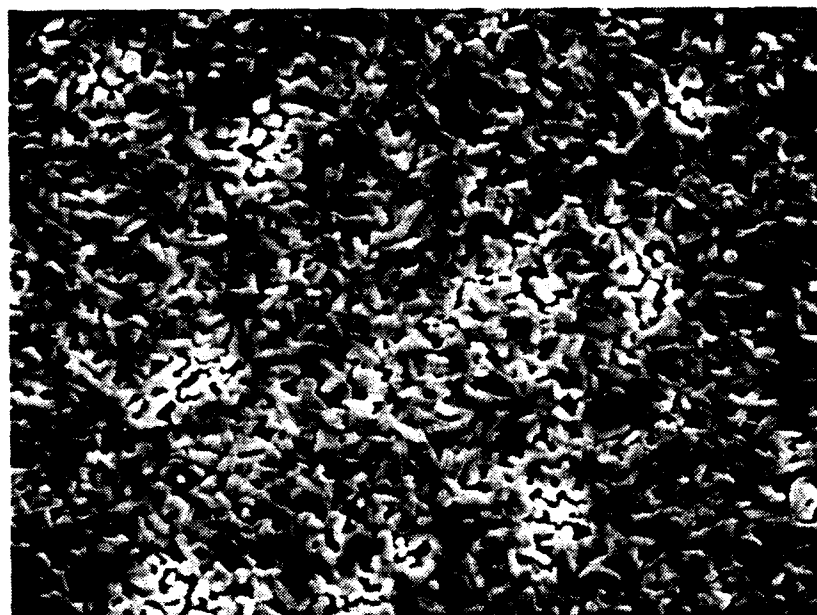


Fig. 14. Surface morphology of Dyl23 film on YSZ (900°C, 10 min)

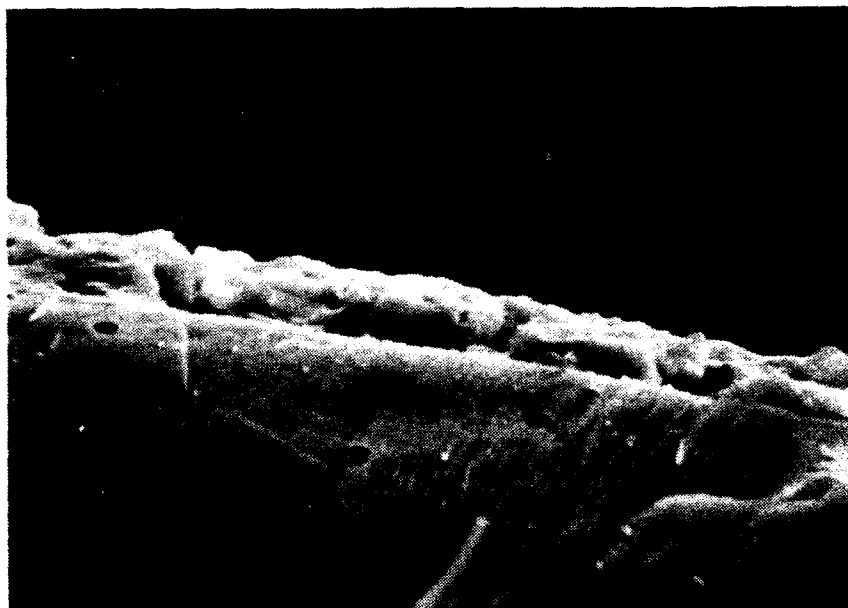


Fig. 15. Y123 film on YSZ with five dippings (915°C, 30 min)

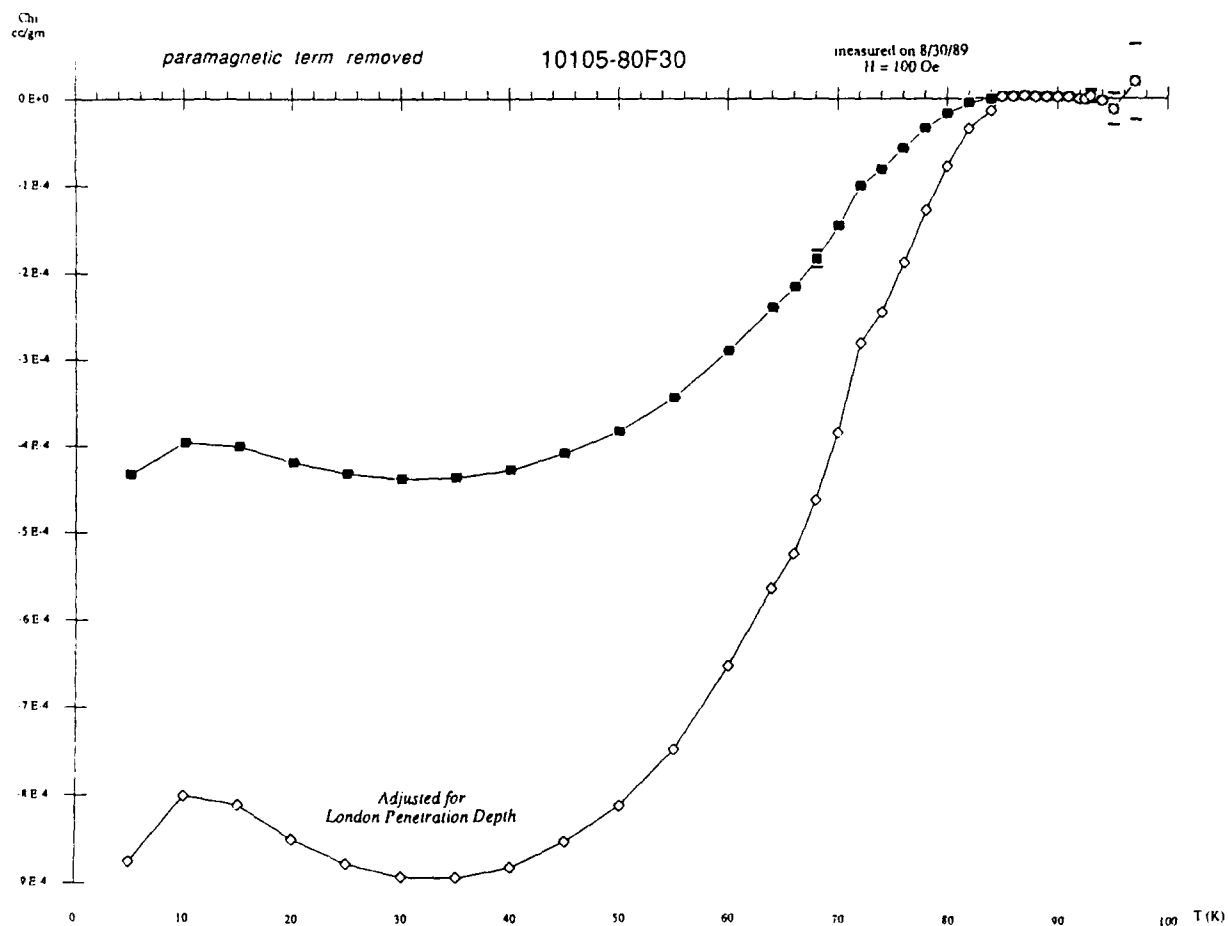


Fig. 16. The dc magnetic susceptibility of Y123 film on YSZ

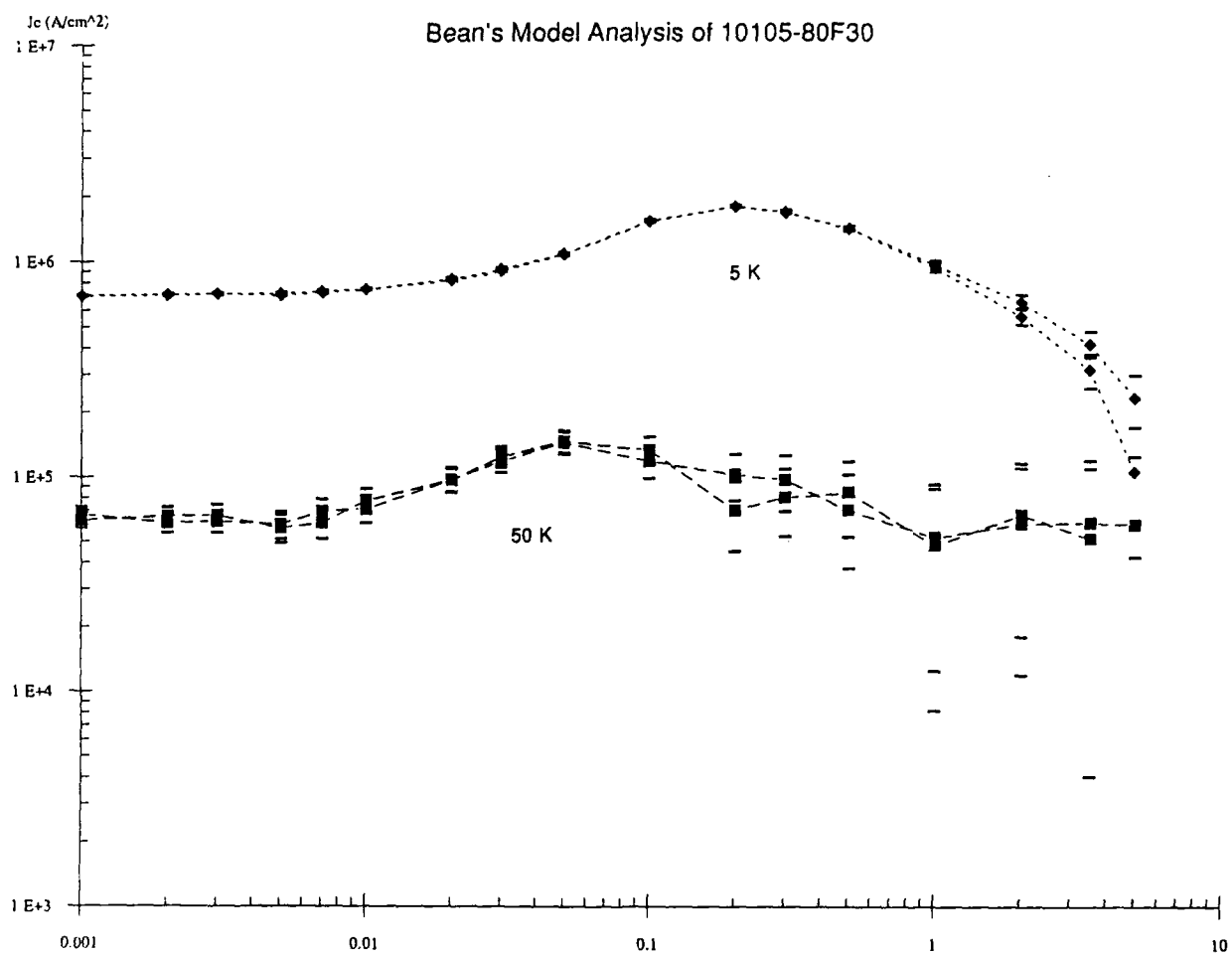


Fig. 17. Critical current densities of Y123 film on YSZ at 5 and 50 K using Bean's model analysis

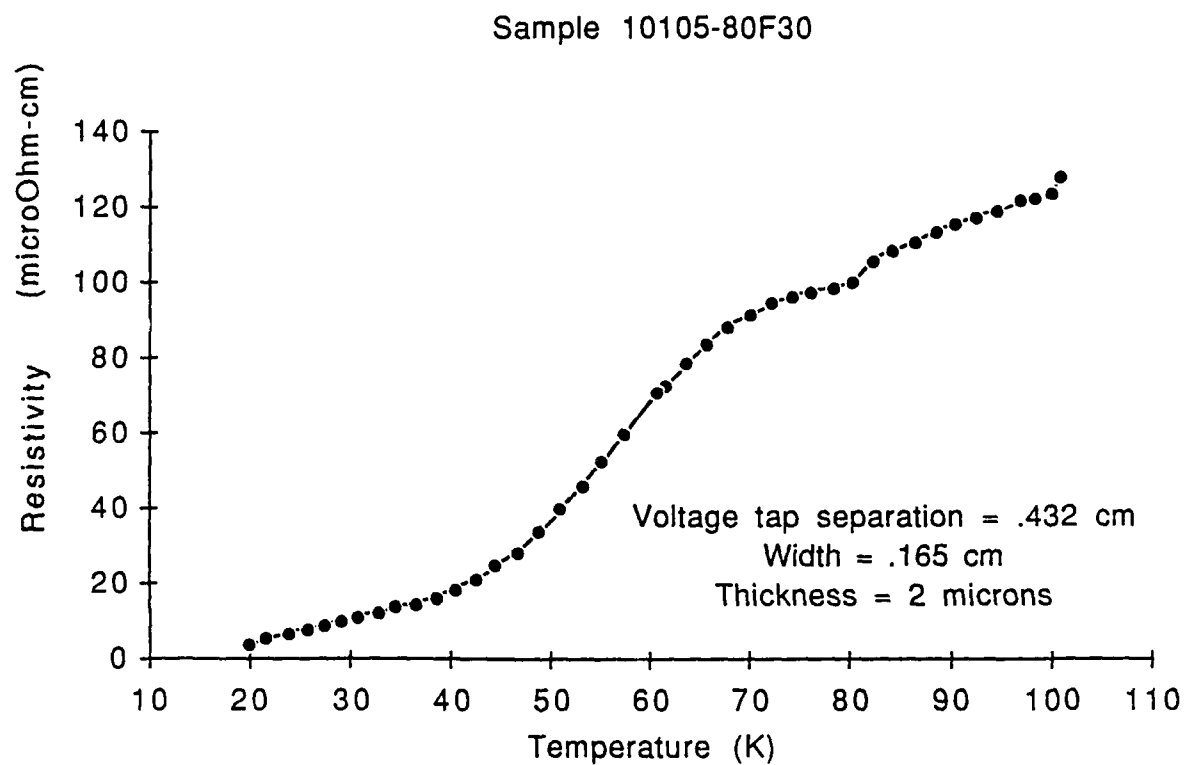


Fig. 18. Resistivity versus temperature plot of Y123 film on YSZ



#### 4. FORMATION OF MICRO-INHOMOGENEITY FOR FLUX PINNING CENTERS

In the previous reports, efforts were made to improve the solution stoichiometry as well as to eliminate the formation of  $\text{BaCO}_3$  through modification of the solution chemistry. The stoichiometry of the solutions and phase purity of  $\text{YBa}_2\text{Cu}_3\text{O}_{7-x}$  ceramics have been much improved as shown by X-ray and differential thermal analysis (DTA) results. In a recent report, Murakami (Ref. 1) has improved critical current density of usually low  $J_c$  bulk YBCO superconductor ceramics to  $1000 \text{ A/cm}^2$  in a magnetic field of 10 Tesla by developing a quench and melt grown phase process. This process generates submicron size  $\text{Y}_2\text{BaCuO}_5$  (211) crystallites uniformly dispersed inside  $\text{YBa}_2\text{Cu}_3\text{O}_{7-x}$  grains. The relatively high  $J_c$  in a strong magnetic field indicated that 211 crystallites may act as flux pinning centers. In view of this result, it was decided to adjust the composition of the solutions used in this program so as to incorporate some 211 phase in the final superconducting ceramic fibers. Composition of (1)  $\text{YBa}_2\text{Cu}_3\text{O}_{7-x} + 0.02 \text{ Y}_2\text{BaCuO}_5$ ; (2)  $\text{YBa}_2\text{Cu}_3\text{O}_{7-x} + 0.03 \text{ Y}_2\text{BaCuO}_5$ ; (3)  $\text{YBa}_2\text{Cu}_3\text{O}_{7-x} + 0.05 \text{ Y}_2\text{BaCuO}_5$ ; and (4)  $\text{YBa}_2\text{Cu}_3\text{O}_{7-x} + 0.10 \text{ Y}_2\text{BaCuO}_5$  have been prepared. The intention is to see if finely-dispersed 211 phase can be introduced by sol-gel process.

The X-ray diffraction of the Y123 fibers made from these solutions are shown in Figs. 19(a) through 19 (d). The microstructure of these fiber and their electrical properties in magnetic field is in progress.

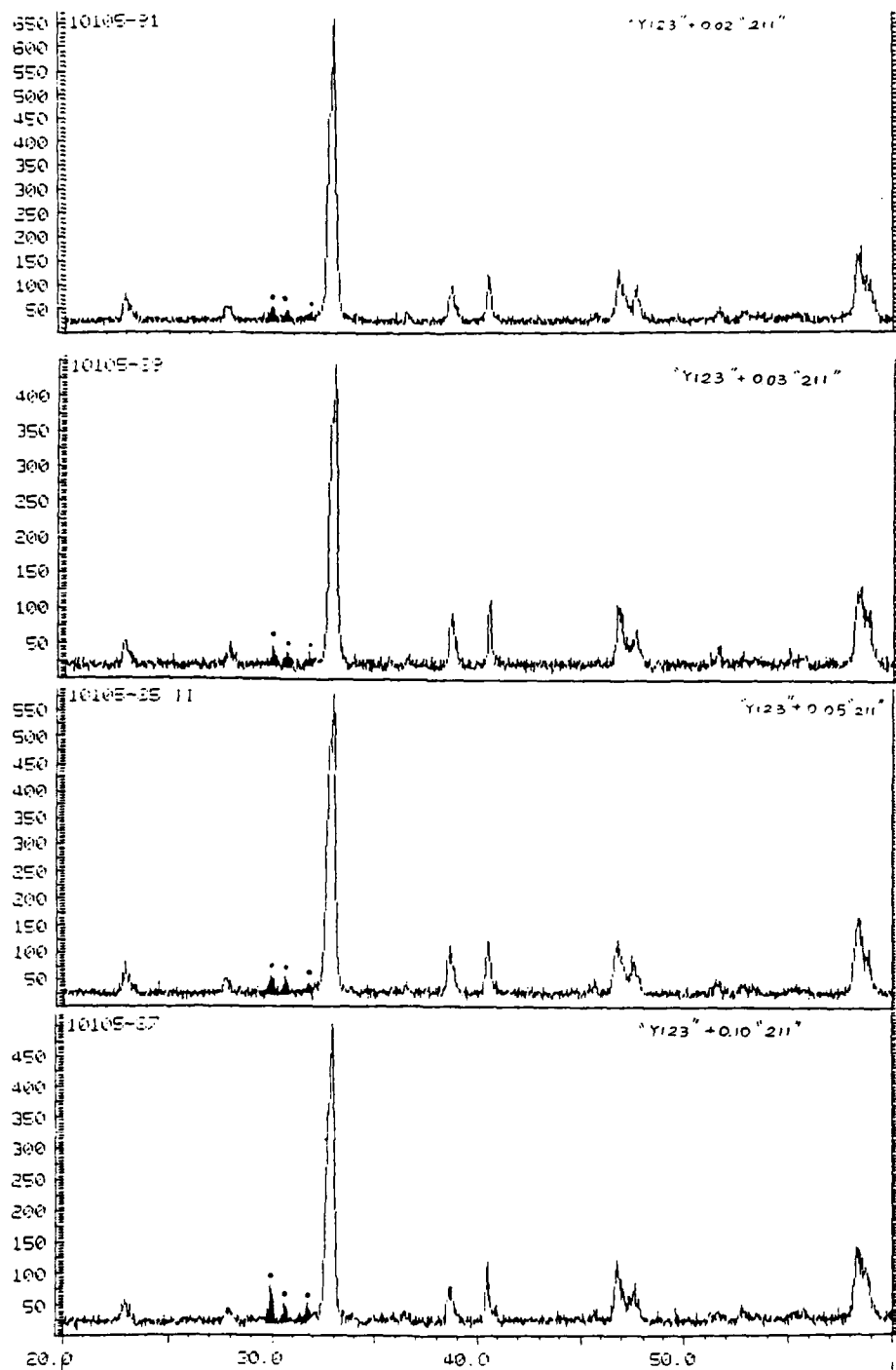


Fig. 19. X-ray diffractions of Y123 fibers with different amount of  $\text{Ba}_2\text{YCuO}_5$  addition: (a) "123" + 0.02 "211;" (b) "123" + 0.03 "211;" (c) "123" + 0.05 "211;" and (d) "123" + 0.10 "211"

## 5. FIBER PREFERRED CRYSTALLOGRAPHIC-ORIENTATION (TEXTURING)

The preferred crystallographic-orientation of 123 fiber with assistance of magnetic field alignment in presence of Dy123 seeds was initiated. In the preliminary study, the 0.0066 grams of fine  $\text{DyBa}_2\text{CuO}_{7-x}$  seeds, prepared by calcining the solution-coated paper filaments at  $900^\circ\text{C}$  for 2 h, were incorporated into 0.22 grams of viscous solution of Y123 composition. Fibers were hand-drawn from this solution and passed through 0.75 T magnetic field. The fibers were sintered at  $875^\circ\text{C}$  for 5 h and then  $950^\circ\text{C}$  for 8 h. The purpose of unusually long firing times was in the study to enhance the grain growth in order to see if any grain alignment has been achieved. The microstructure of the fiber prepared by this technique is shown in Figs. 20(a) through 20(c). Plate-like habit growth of the (Y,Dy)123 crystals are seen, however, no preferred grain orientation was observed. The preliminary lack of preferred grain orientation in the fiber may have been due to any single or combined parameters, such as the viscosity of the solution, the time of the fiber in the magnetic field, the magnetic field strength needed for grain alignment, and the uniform dispersion of the Dy123 seeds. It may also be that the homogeneous nucleation in the fibers prevails over heterogeneous epitaxial growth on the aligned Dy123 seeds.

During the next period attempts will be made to optimize the aforementioned parameters and have answers to most of the questions in regard to grain orientation problems affecting the critical current density.

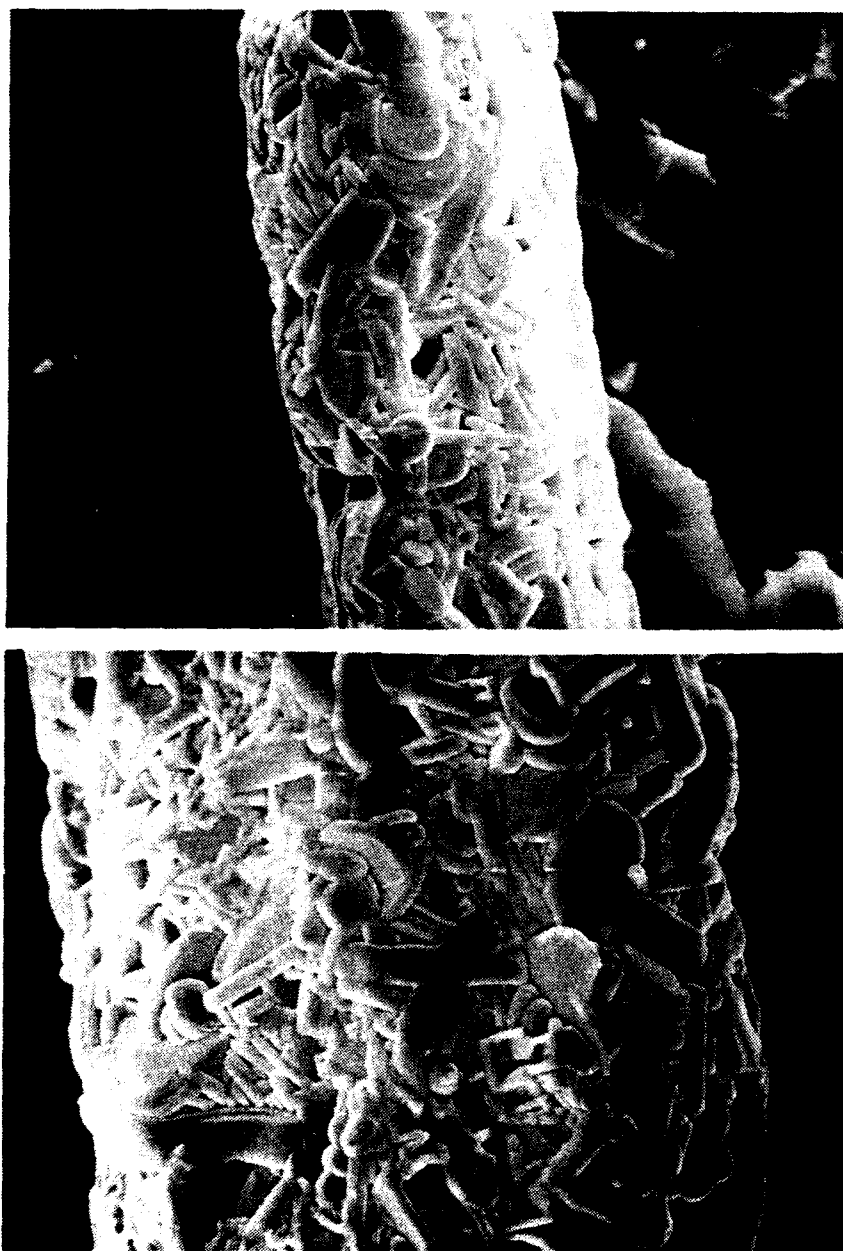


Fig. 20. SEM micrographs of seeded Y123 fibers (sheet 1 of 2)

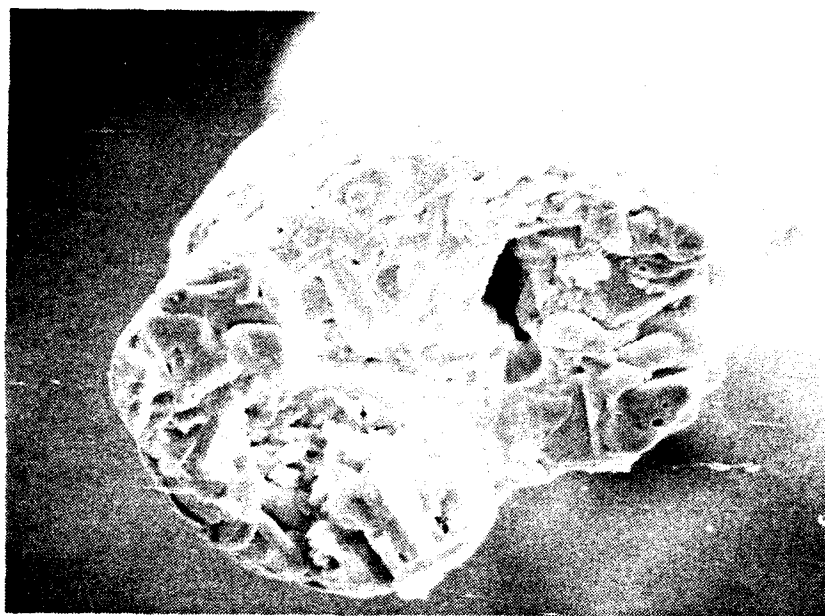


Fig. 20. SEM micrographs of seeded Y123 fibers (sheet 2 of 2)

## 6. CAVITY Q FACTOR MEASUREMENTS

The room temperature Q of the gold plated  $TE_{011}$  cavity was raised from 14,000 to 21,000 by replating and repolishing the top plate. This is considered a reasonable value, quite high enough to measure the surface resistance of our films. The liquid helium dewar is being built at Precision Cryogenic Systems. All of the other parts needed for the cryogenic measurements are in house, and the top flange with the feed-throughs for the coaxial cables, wires for temperature sensors and heaters, and tubing for pumping air out has been made. The final integration of the cryostat will be done when the dewar arrives.

## 7. REFERENCE

1. Murakami, M., "Microstructure and Critical Current Density of Ceramic Superconductors," Bulletin of the Ceramic Society of Japan 24 [8], 704-709 (1989).

APPENDIX  
FLUX BUNDLE INTERACTIONS



# Flux Bundle Interactions

Richard B. Stephens  
General Atomics

## Abstract

We have shown that magnetic flux lattice interactions are important at fields above a few hundred gauss and temperatures below 40 K. These interactions interfere with thermally activated current-induced flux bundle hopping and reduces the superconductor's flux creep resistance below that estimated from the standard flux creep models (which assume completely independent hopping). As a result, the optimum pinning site density for low temperature applications in that region is that in which the pinning site separation approximately matches the spacing of the flux bundle lattice. For applications above 40 K, thermal activation reduces the effect of lattice interaction upon the motion of flux bundles, and the independent hopping model is probably a good description. In that region one minimizes creep resistance by maximizing the pinning center density.

# Flux Bundle Interactions

Richard B. Stephens  
General Atomics

## Introduction

Flux creep, which is hard to detect in older type II superconductors<sup>1,2</sup>, is apparently the dominant effect in limiting the current carrying capability of the ceramic oxide superconductors<sup>3</sup>. Their shorter coherence length leads to a weaker flux pinning energy, while operation at higher temperatures gives the flux bundles considerably more thermal energy. Thermally activated hopping of flux bundles is therefore much more rapid than in the older materials.

This phenomenon has been analyzed from two very different points of view. A spin glass model was originally proposed.<sup>4</sup> Subsequently, a large number of people have applied the Anderson - Kim model of flux hopping<sup>5</sup>. In the former model, the interaction between flux bundles is so strong that several bundles must move in a coordinated fashion during a relaxation event. The latter model assumes flux bundles interact very weakly and hop independently of their neighbors.

The purpose of this paper is to delineate the boundary between the two descriptions and to describe its effect on flux creep resistance.

## Qualitative Description

We will define the boundary between cooperative and independent flux hopping using a minimal array of flux bundles — one bundle surrounded by six neighboring bundles at the equilibrium distance (in the absence of current)

---

<sup>1</sup>A.M. Campbell & J.E. Evetts, "Flux vortices and transport currents in type II superconductors," *Adv. Phys.* **21**, 199 (1972)

<sup>2</sup>M.R. Beasley, R. Labusch, & W.W. Webb, "Flux creep in type II superconductors," *Phys. Rev.* **181** 682 (1969).

<sup>3</sup>K.A. Müller, M. Takashige, and J.G. Bednorz, *Phys. Rev. Lett.* **58** 1143 (1987).

<sup>4</sup>C. Rossel, Y. Maeno, and I. Morgenstern, "Aging effects in superconducting Y-Ba-Cu-O single crystal: a similarity with spin-glasses," *Phys. Rev. Lett.* **89**

<sup>5</sup>Y. Yeshurun & A.P. Malozemoff, "Giant flux creep and irreversibility in an Y-Ba-Cu-O crystal: An alternative to the superconducting glass model," *Phys. Rev. Lett.* **21** 2022 (1988).

$$r = \lambda \sqrt{\frac{H_{c1}}{H}} \quad (1)$$

where  $\lambda$  is the magnetic field penetration length,  $H_{c1}$  is the lower critical field, and  $H$  is the applied field.

The flux bundles are pinned, but we assume that the density of pinning sites is so high that that does not affect the configuration of the flux lattice (separation between pinning sites,  $d$ , much less than  $r$ ). We then turn on a transverse current density  $J$ . The pinning sites (with pinning energy  $U$ ), current, and neighbors interact with the central flux bundle to produce a free energy which varies with position as shown in Figure 1.

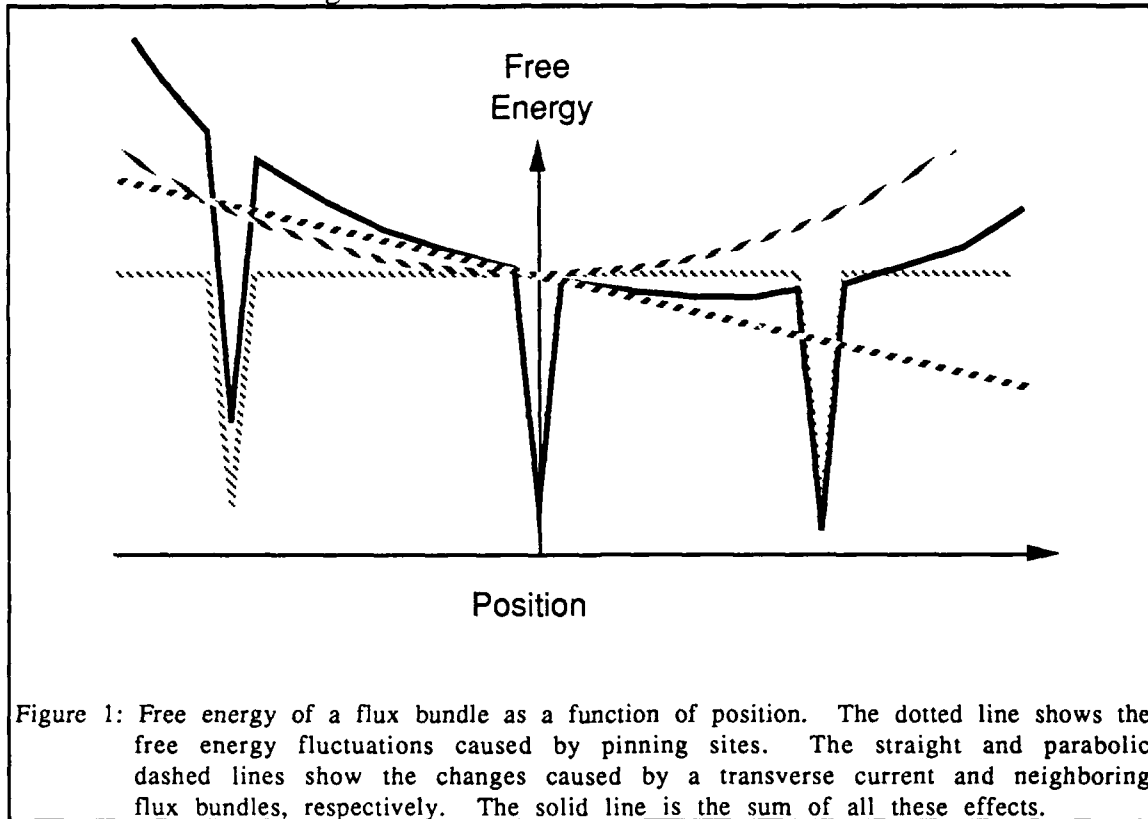


Figure 1: Free energy of a flux bundle as a function of position. The dotted line shows the free energy fluctuations caused by pinning sites. The straight and parabolic dashed lines show the changes caused by a transverse current and neighboring flux bundles, respectively. The solid line is the sum of all these effects.

Thermally generated fluctuations cause the flux bundle to periodically jump out of its pinning site. On such a jump the Lorentz force from the current tends to drive the flux bundles to the right, reducing the energy at the right hand side by  $U_J$ , but interaction with the surrounding lattice,  $U_{int}$ , resists those hops. The dynamics of the flux lattice depends on the relative sizes of these three energies:

- The interaction energy reduces the individual hopping rate when  $U_{int} > kT$  or  $U_{int} > U_J$ .

- The interaction energy reduces the rate of individual hopping to less than that of coordinated hopping of multiple bundles (spin glass behavior) when  $U_{\text{int}} > U$ .
- If  $kT > U_{\text{int}}$  even for hopping distances a large fraction of the flux bundle lattice constant, then the bundle positions will be essentially random, and the lattice will "melt".

### Flux Lattice Interaction

This qualitative discussion can be made quantitative:  
The interaction energy (per unit length) between two quanta of flux in an extreme type II superconductor is<sup>1</sup>:

$$E_{\text{int}} = \frac{\Phi_0^2}{8\pi^2\lambda^2\mu_0} K_0(r/\lambda). \quad (2)$$

For  $a \equiv r/\lambda \gg 1$  the limiting form is

$$K_0(a) = \left(\frac{\pi}{2a}\right)^{\frac{1}{2}} e^{-a} \quad (3)$$

and

$$\frac{d}{da} K_0(a) = -\left(1 + \frac{1}{2a}\right) \left(\frac{\pi}{2a}\right)^{\frac{1}{2}} e^{-a} \quad (4)$$

$$\frac{d^2}{da^2} K_0(a) = \left(1 + \frac{1}{a} + \frac{3}{4a^2}\right) \left(\frac{\pi}{2a}\right)^{\frac{1}{2}} e^{-a} . \quad (5)$$

$$K_0(a) = 0.12 - \ln(a) \quad (6)$$

$$\frac{d}{da} K_0(a) = -\frac{1}{a} \quad (7)$$

$$\frac{d^2}{da^2} K_0(a) = \frac{1}{a^2} . \quad (8)$$

One can see from Figure 2 that the two analytic forms diverge from  $K_0(a)$  at  $a \approx 0.5$ . Within their regimes, the analytic forms have errors of 10 - 50% at worst, and that only over a factor of 2 near the break point. The first derivatives are continuous at the breakpoint, and the second derivatives different by  $\approx 30\%$

---

<sup>1</sup>M. Tinkham Introduction to Superconductivity (McGraw Hill, New York, 1975)

Expanding the interaction function

$$K_0(r+s) = K_0(r) + s K_0'(r) + \frac{1}{2} s^2 K_0''(r) + \dots$$

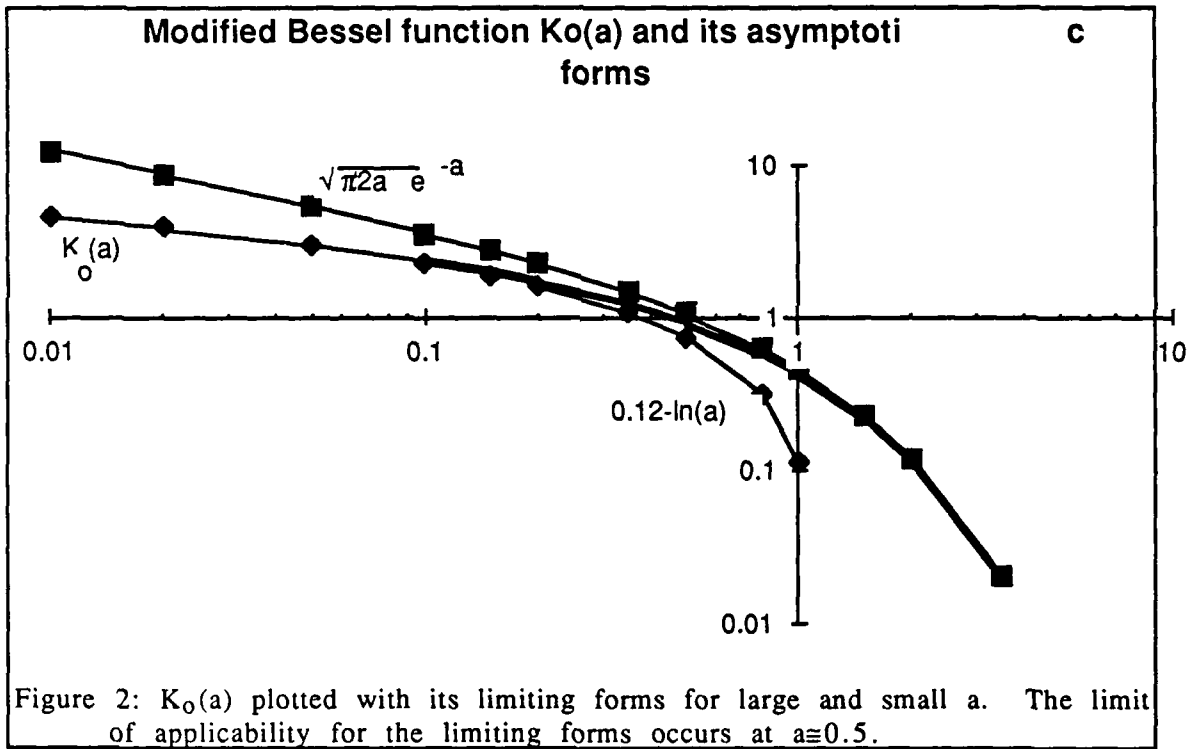
so

$$\frac{\Delta K_0(r)}{K_0(r)} \cong -s \left( 1 + \frac{1}{2a} \right) + \frac{1}{2} s^2 \left( 1 + \frac{1}{a} + \frac{3}{4a^2} \right) \quad (9a)$$

for  $a > 0.5$  and

$$\frac{\Delta K_0}{K_0} \cong -\frac{s}{a} + \frac{1}{2} \left( \frac{s}{a} \right)^2 \quad (9b)$$

for  $a < 0.5$ .

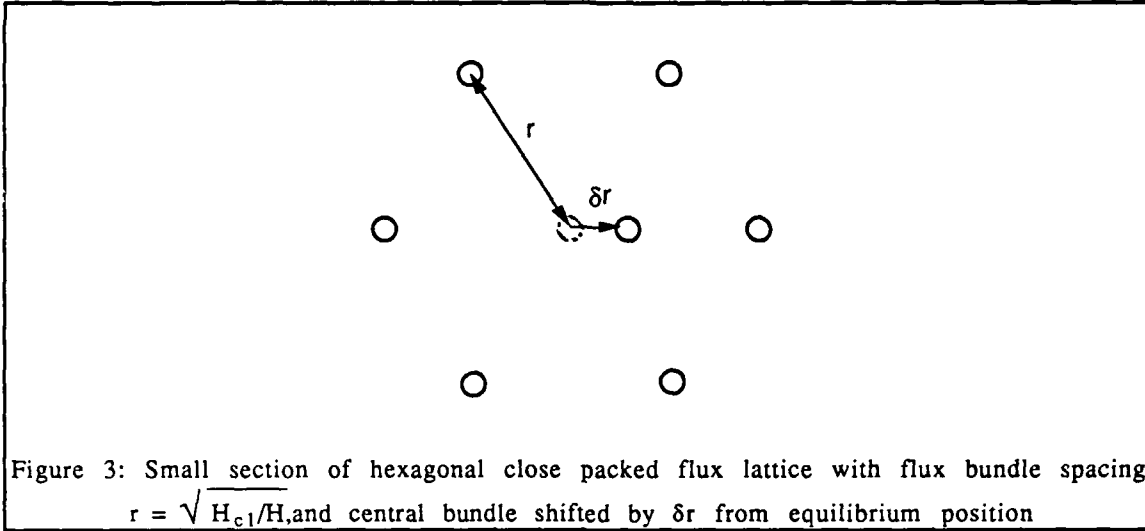


Take a hexagon of flux bundles surrounding a central bundle (Figure 3), and move the central one by  $\delta r$  toward one of its neighbors. The distances to its six neighbors change by factors

$$1 \pm \delta \quad (10a)$$

$$\sqrt{1 \pm \delta + \delta^2} \cong 1 \pm \frac{1}{2} \delta + \frac{3}{8} \delta^2 \quad (10b)$$

where there are two neighbors whose distance change by the each of the factors given by 10b.



The change in free energy of the central bundle resulting from this shift is the sum of the changes over the six neighbors

$$\Delta E_{\text{int}} \equiv \frac{\Phi_0^2}{8\pi^2\lambda^2\mu_0} K_0(a) \left\{ -\frac{\delta r}{\lambda} \left(1 + \frac{1}{2a}\right) + \frac{1}{2} \left(\frac{\delta r}{\lambda}\right)^2 \left(1 + \frac{1}{a} + \frac{3}{4a^2}\right) \right. \\ \left. + \frac{\delta r}{\lambda} \left(1 + \frac{1}{2a}\right) + \frac{1}{2} \left(\frac{\delta r}{\lambda}\right)^2 \left(1 + \frac{1}{a} + \frac{3}{4a^2}\right) \right. \\ \left. + 2 \left( \frac{1}{2} \frac{\delta r}{\lambda} + \frac{3}{8} \left(\frac{\delta r}{\lambda}\right)^2 \right) \left(1 + \frac{1}{2a}\right) + \frac{1}{4} \left(\frac{\delta r}{\lambda}\right)^2 \left(1 + \frac{1}{a} + \frac{3}{4a^2}\right) \right. \\ \left. + 2 \left( -\frac{1}{2} \frac{\delta r}{\lambda} + \frac{3}{8} \left(\frac{\delta r}{\lambda}\right)^2 \right) \left(1 + \frac{1}{2a}\right) + \frac{1}{4} \left(\frac{\delta r}{\lambda}\right)^2 \left(1 + \frac{1}{a} + \frac{3}{4a^2}\right) \right\} \quad (11a)$$

$$\Delta E_{\text{int}} \equiv \frac{\delta^2 r^2 \Phi_0^2}{8\pi^2\lambda^4\mu_0} \left( \frac{7}{2} + \frac{1}{4a} + \frac{3}{2a^2} \right) \left( \frac{\pi}{2a} \right)^{\frac{1}{2}} e^{-a} \quad (11b)$$

for  $a > 0.5$  to second order in  $\delta$ , and the energy is given per unit length of bundle. A similar expansion of the small  $a$  form gives

$$\Delta E_{\text{int}} \equiv \frac{\Phi_o^2}{8\pi^2\lambda^2\mu_o} K_o(a) \left\{ -\frac{\delta r}{\lambda} \left( \frac{1}{a} \right) + \frac{1}{2} \left( \frac{\delta r}{\lambda} \right)^2 \left( \frac{1}{a^2} \right) \right. \\ \left. + \frac{\delta r}{\lambda} \left( \frac{1}{a} \right) + \frac{1}{2} \left( \frac{\delta r}{\lambda} \right)^2 \left( \frac{1}{a^2} \right) \right. \\ \left. + 2 \left( \frac{1}{2} \frac{\delta r}{\lambda} + \frac{3}{8} \left( \frac{\delta r}{\lambda} \right)^2 \right) \left( \frac{1}{a} \right) + \frac{1}{4} \left( \frac{\delta r}{\lambda} \right)^2 \left( \frac{1}{a^2} \right) \right. \\ \left. + 2 \left( -\frac{1}{2} \frac{\delta r}{\lambda} + \frac{3}{8} \left( \frac{\delta r}{\lambda} \right)^2 \right) \left( \frac{1}{a} \right) + \frac{1}{4} \left( \frac{\delta r}{\lambda} \right)^2 \left( \frac{1}{a^2} \right) \right\} \quad (12a)$$

$$\Delta E_{\text{int}} \equiv \frac{\delta^2 r^2 \Phi_o^2}{8\pi^2\lambda^4\mu_o} \left( \frac{3}{2a} + \frac{2}{a^2} \right) (0.12 - \ln(a)) \quad (12b)$$

At the break point of  $a = 0.5$ , Eqns 11b and 12b are 16.1 and 7.7 respectively, excluding the first fraction. That suggests the error is about 50% at that point, as expected by inspection of the errors in the approximations to  $K_o(a)$ .

Given a current through the superconductor, there is a transverse force  $\mathbf{J} \times \mathbf{B}$  on the flux bundles which tends to force the bundles to the right. This motion is significantly reduced when the increase in interaction energy on a single hop,  $\Delta E_{\text{int}} d > kT$ . It is reduced to less than that of cooperative movement of multiple bundles when  $\Delta E_{\text{int}} d > U$ . (We have taken  $d$  to be the length of flux that moves on a single hop. Writing these relations out in detail, the boundaries between independent flux motion and single hopping in a flux lattice, and between single hops and cooperative motion in a flux lattice occur at:

$$kT = \frac{\Phi_o H_c d^3}{8\pi\lambda^2\mu_o} \left( \frac{7}{2} + \frac{1}{4a} + \frac{3}{2a^2} \right) \left( \frac{\pi}{2a} \right)^{\frac{1}{2}} e^{-a} \quad a > 0.5 \quad (13a)$$

$$kT = \frac{\Phi_o H_c d^3}{8\pi\lambda^2\mu_o} \left( \frac{3}{2a} + \frac{2}{a^2} \right) (0.12 - \ln(a)) \quad a < 0.5 \quad (13b)$$

and

$$U = \frac{\Phi_o H_c d^3}{8\pi\lambda^2\mu_o} \left( \frac{7}{2} + \frac{1}{4a} + \frac{3}{2a^2} \right) \left( \frac{\pi}{a} \right)^{\frac{1}{2}} e^{-a} \quad a > 0.5 \quad (14a)$$

$$U = \frac{\Phi_o H_c d^3}{8\pi\lambda^2\mu_o} \left( \frac{3}{2a} + \frac{2}{a^2} \right) (0.12 - \ln(a)) \quad a < 0.5 \quad (14b)$$

respectively, where  $d = \delta r$ ,  $H_{c1} = \Phi_0/\pi\lambda^2$ .

Note that one can use Eqn. 13 to define the distance a flux bundle can move from its equilibrium position,  $\Delta r_{kT}$ , before being affected by its neighbors:

$$\Delta r_{kT} = \sqrt{\frac{8\pi\mu_0 k T \lambda^2}{\Phi_0 H_{c1} d} \left( \frac{7}{2} + \frac{1}{4a} + \frac{3}{2a^2} \right)^{-1} \left( \frac{a}{2\pi} \right)^{\frac{1}{2}} e^a} \quad r > 0.5 \quad (15a)$$

$$\Delta r_{kT} = \sqrt{\frac{8\pi\mu_0 k T \lambda^2}{\Phi_0 H_{c1} d} \left( \frac{3}{2a} + \frac{2}{a^2} \right)^{-1} (0.12 - \ln(a))^{-1}} \quad r < 0.5 \quad (15b)$$

When  $\Delta r_{kT}/r \geq 0.2$ , one would expect the lattice to melt.<sup>1</sup>

$$T_{\text{melt}} = .04 \frac{\Phi_0 d H_{c1}}{8\pi k \mu_0} a^2 \left( \frac{7}{2} + \frac{1}{4a} + \frac{3}{2a^2} \right) \left( \frac{\pi}{2a} \right)^{\frac{1}{2}} e^{-a} \quad r > 0.5 \quad (16a)$$

$$T_{\text{melt}} = .04 \frac{\Phi_0 d H_{c1}}{8\pi k \mu_0} a^2 \left( \frac{3}{2a} + \frac{2}{a^2} \right) (0.12 - \ln(a)) \quad r < 0.5 \quad (16a)$$

The behavior described above assumes that a flux bundle's neighbors are pinned at their equilibrium distances when it attempts to hop. At temperatures such that  $U \approx kT$ , there is a probability  $P = e^{-U/kT}$  that a given neighbor is free at the time of a hop. When half of them are free, ( $T = 3U/k \ln 40$ ) one may assume that the lattice interaction is not so likely to interfere with independent hopping; in that case, several neighbors are free to move in a coordinated fashion to share the interaction energy.

### Flux Lattice Phase Diagram

One has the constants describing the permeability of space and flux quantization:

$$\mu_0 = 4\pi \times 10^{-7}$$

$$\Phi_0 = 2.07 \times 10^{-15} \text{ T-m}^2$$

For the 123 family of ceramic oxide superconductors the zero temperature parameters are,

$$\lambda \approx 2 \times 10^{-7} \text{ m}$$

$$H_{c1} \approx 10^{-2} \text{ T}$$

$$U = 2 \times 10^{-2} \text{ eV}$$

and we estimate the pinning site distance to be

$$d \approx 10^{-8} \text{ m}$$

Then the prefactors above are

---

<sup>1</sup>Lindemann criterion



$$\frac{\Phi_0 H_{c1} d^3}{8\pi\lambda^2\mu_0} = 6.6 \times 10^{-23} \text{ J} \cong 4.8 \text{ K} \cong 4.1 \times 10^{-4} \text{ eV}$$

for Eqns 13 & 14, and

$$.04 \frac{\Phi_0 d H_{c1}}{8\pi k \mu_0} = 19 \text{ K}$$

for Eqn 16.

The high temperature limit for lattice interactions is  
 $T = 39 \text{ K}$ .

From these calculations, one can draw the flux lattice phase diagram shown in Figure 4. We have not included any temperature dependence of the superconducting parameters. In the clear region at the bottom, the interaction between flux bundles is so weak that they cannot maintain a hexagonal lattice. In the shaded region, the interaction energy is large enough to significantly reduce the hopping rate from that of independent flux bundles. The narrow region in between is an area in which a hexagonal lattice is stable but the single hopping rate is not significantly affected. At  $H = 1 \text{ Tesla}$ , the bundle spacing is the same as the pinning site spacing, and this model breaks down. In that region the interaction is so strong that one has only cooperative hopping.

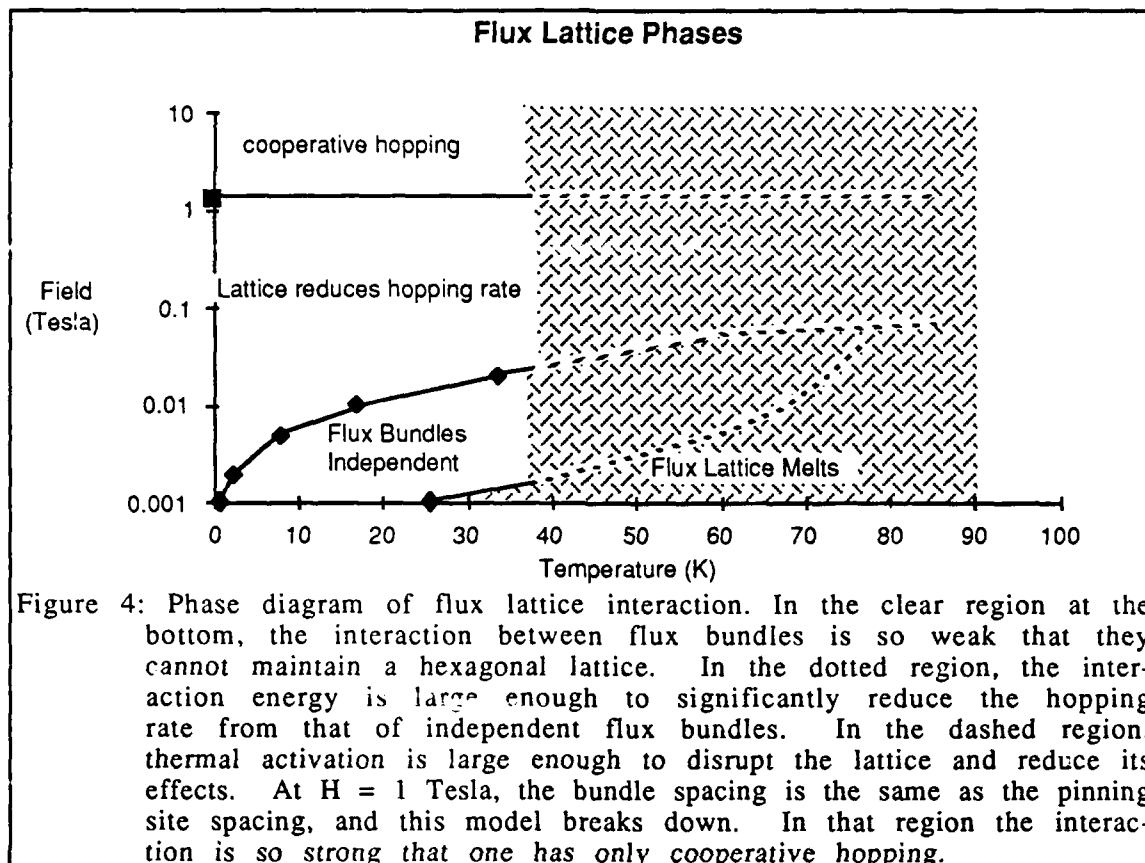


Figure 4: Phase diagram of flux lattice interaction. In the clear region at the bottom, the interaction between flux bundles is so weak that they cannot maintain a hexagonal lattice. In the dotted region, the interaction energy is large enough to significantly reduce the hopping rate from that of independent flux bundles. In the dashed region, thermal activation is large enough to disrupt the lattice and reduce its effects. At  $H = 1$  Tesla, the bundle spacing is the same as the pinning site spacing, and this model breaks down. In that region the interaction is so strong that one has only cooperative hopping.

It appears that SQUID antennae, operating in fields less than  $10^{-4}$  T ( $< 1$  Oe), will have flux bundles which hop independently. The standard flux creep model will apply to that situation using an activation energy which reflects the true pinning energy of a single pinning site.

It also appears that most magnetic coils will operate in a regime where the flux lattice interactions tend to interfere with hopping, but that thermal excitations will substantially reduce that effect. Standard flux creep models will work reasonably well here also.

Only the region in which low temperature and significant magnetic field are combined will exhibit reduced creep.

### Flux Creep Resistance

Previous analyses based on independent flux motion have shown that thermal activation causes a finite electrical resistance in these superconductors. This extension of that work shows that the flux lattice inhibits this hopping somewhat.

To analyze the effects, we separate the hopping process into two parts: first breaking free of the original pinning site, then land-

ing either back in the same site, or in one of its two neighbors. The sum of the probabilities for landing in one of the three pinning sites must add to 1. There may be a shallow minimum in the free energy between the pinning sites, as shown in Figure 1, but the flux bundle should spend very little time there compared to the pinning sites. The average velocity  $\langle v \rangle$  is the product of the attempt frequency,  $\Omega$ , the success rate (the product of the two steps above) and the jump distance,  $+d$ ,  $0$ , and  $-d$ :

$$\langle v \rangle = \Omega d e^{-U/kT} \frac{(e^{-\Delta_+/kT} - e^{-\Delta_-/kT})}{(1 + e^{-\Delta_+/kT} + e^{-\Delta_-/kT})} \quad (17)$$

where  $U$  is the pinning energy, and  $\Delta_+$  and  $\Delta_-$  are the differences in energy between the original pinning site and the neighbors in the forward and reverse direction (direction relative to the Lorentz force) respectively. The denominator normalizes the destination probabilities. The  $\Delta$ 's are the sum of the Lattice interaction energy,  $\Delta E_{int}$ , and the Lorentz energy,  $U_J = J\Phi_0 d^2$ . We know the former is symmetric and the latter asymmetric with respect to the original pinning site. In addition, for low current densities (defined by  $U_J < \Delta E_{int}$ ), the normalization factor in Eqn 17 is  $\approx 1$  and Eqn 17 can be rewritten as

$$\langle v \rangle = 2\Omega d e^{-(U+\Delta E_{int})/kT} \sinh(J\Phi_0 d^2/kT) \quad (18)$$

The back electric field,  $E$ , caused by this flux flow is  $B\langle v \rangle$ . With the assumption that the argument of the sinh is small (e.g. large temperature and/or small currents), that term may be linearized so that

$$E = 2B\Omega d J\Phi_0 d^2/kT e^{-(U+\Delta E_{int})/kT} \quad (16)$$

Assuming the pinning centers are triangular wells of depth  $U$  and opening  $\xi$ , the shape of the well distorts, and the pinning energy (the difference in energy between the well's lower edge and its bottom decreases with increasing  $J$ . At  $J_{c0}$  the pinning energy goes to zero, and flux moves freely even in the absence of thermal activation. Hence:

$$J_{c0} = U/\Phi_0 d \xi. \quad (17)$$

Eqn 15 finally becomes

$$\rho = E/J = E_0/J_{c0} d/\xi U/kT e^{-(U+\Delta E_{int})/kT} \quad (18)$$

where  $E_0 \equiv B\Omega d$

Eqn 18 is the similar to that previously derived except for the addition of an interaction term which rapidly grows with field and is greater than  $kT$  (hence has more than a factor of 3 effect in the measured resistance) in the shaded area in Figure 4.

### Optimum pinning density

It is interesting to look at the dependence of  $\rho$  on pinning site spacing,  $d$ . Increasing  $d$  forces a bundle to hop closer to its neighbors in order to get to a pinning site. The repulsion between neighbors should make such jumps less frequent, which may offset the increased motion on a successful jump. In the limit that the pinning site spacing,  $d$ , is the same as the flux bundle spacing,  $r$ , this model breaks down; it assumes that the central bundle must hop exactly to its neighbor to get to the next pinning site. We must therefore limit the  $d$  to  $d < r/2$ .

For this analysis we take the environment

$$H = 1 \text{ T},$$

$$J = 10^4 \text{ A/cm}^2, \text{ and}$$

$$T = 50 \text{ K}.$$

The superconducting parameters are:

$$\xi = 10^{-9} \text{ m}$$

$$U = 2 \times 10^{-2} \text{ eV}$$

$$\lambda = 10^{-5} \text{ m}$$

$$\Omega = 10^6 \text{ s}^{-1}$$

$$H_{c1} = 10^{-2} \text{ T}$$

Derived parameters are:

$$U/kT = 4.64$$

$$r = \lambda \sqrt{H_{c1}/H} = \lambda/10 = 10^{-8} \text{ m}$$

To keep the variable dimensionless, I use  $d/r$  as the variable:

$$J_{co} = U/\Phi_0 d \xi = 1.55 \times 10^{11} \text{ A/m } (r/d)$$

$$E_0 = B \Omega d = 10^{-2} \text{ V } (d/r)$$

$$\Delta E_{int} = 49 (d/r)^3$$

$$d/\xi = 10 \text{ } d/r$$

For reference, useful constants are:

$$\Phi_0 = 2.07 \times 10^{-15} \text{ T-m}^2$$

$$\mu_0 = 4 \pi \cdot 10^{-7}$$

$$k_B = 1.38 \times 10^{-23} \text{ J/K}$$

$$1 \text{ J} = 6.24 \times 10^{18} \text{ eV}$$

then Eqn 18 can be rewritten as:

$$\rho = 2.9 \times 10^{-14} \text{ } \Omega\text{-m} \left( \frac{d}{r} \right)^3 e^{-49(d/r)^3} \quad (19)$$

The exponential form comes from the flux lattice interaction. Writing the resistance in this form, it is clear that the resistance increases with  $d$  only so long as there is no lattice interaction. As soon as  $d$  is large enough that the exponential term becomes significant, the resistance drops dramatically. As mentioned above, the approximations used in this analysis break down for  $d/r > 0.5$ , and for temperatures large enough that the lattice is thermally excited out of its pinning sites. For  $d/r > 1$  some fraction of the flux bundles are permanently unpinning, and flux shear tends to increase the resistance again. For  $T > 39$  K (for  $U = 0.02$  eV), half of a flux bundle's neighbors are unpinning at any instant, and the resistance to motion is substantially decreased.

One can conclude then that matching the distance between the pinning sites to the anticipated separation between flux bundles can cause significant improvements in the low temperature superconductor behaviour. For applications involving fields around 1 Tesla, the pinning sites should be separated by about  $10^{-8}$  m ( $\approx 100$  Å). Flux decoration experiments by Dolan<sup>1</sup> suggest that the upper limit for the pin spacing is only slightly larger than that. For high temperature applications ( $T > 40$  K), thermal activation limits the restraint on flux motion caused by the lattice, and one wishes the pinning density to be as high as possible.

## Summary

We have shown that magnetic flux lattice interactions are significant at fields above a few hundred gauss and temperatures below 40 K. These interactions interfere with thermally activated current-induced flux bundle hopping and reduces the superconductor's flux creep resistance below that estimated from the standard flux creep models which assume completely independent hopping. As a result, the optimum pinning site density for low temperature applications is that in which the pinning site separation approximately matches the spacing of the flux bundle lattice. For applications above 40 K, thermal activation reduces the effect of lattice interaction upon the motion of flux bundles, and the independent hopping model is probably a good description.

## Acknowledgement

Discussions with Y.R. Lin-Liu helped to clarify this exposition.

---

<sup>1</sup>G.J. Dolan, G.V. Chandrashekhar, T.R. Dinger, C. Feild, and F. Holtzberg, "Vortex structure in  $\text{YBa}_2\text{Cu}_3\text{O}_7$  and evidence for intrinsic pinning," Phys. Rev. Lett. **62** 827 (1989).